

1 **Large contribution of meteorological factors to inter-decadal**
2 **changes in regional aerosol optical depth**

3 Huizheng Che^{1*}, Ke Gui^{1,2}, Xiangao Xia^{3,2}, Yaqiang Wang¹, Brent N. Holben⁴, Philippe Goloub⁵,
4 Emilio Cuevas-Agulló⁶, Hong Wang¹, Yu Zheng^{7,1}, Hujia Zhao¹, Xiaoye Zhang^{1*}

5
6 1 State Key Laboratory of Severe Weather (LASW) and Key Laboratory of Atmospheric
7 Chemistry (LAC), Chinese Academy of Meteorological Sciences, CMA, Beijing, 100081,
8 China

9 2 College of Earth and Planetary Sciences, University of Chinese Academy of Sciences,
10 Beijing, 100049, China

11 3 Key Laboratory for Middle Atmosphere and Global Environment Observation (LAGEO),
12 Institute of Atmospheric Physics, Chinese Academy of Sciences, Beijing, 100029, China

13 4 NASA Goddard Space Flight Center, Greenbelt, MD, USA

14 5 Laboratoire d'Optique Atmosphérique, Université des Sciences et Technologies de Lille,
15 59655, Villeneuve d'Ascq, France

16 6 Centro de Investigación Atmosférica de Izaña, AEMET, 38001 Santa Cruz de Tenerife, Spain

17 7 Collaborative Innovation Center on Forecast and Evaluation of Meteorological Disasters,
18 Nanjing University of Information Science & Technology, Nanjing 210044, China

19 *Correspondence to:* Huizheng Che (chehz@cma.gov.cn) & Xiaoye Zhang (xiaoye@cma.gov.cn)

20 Abstract

21 Aerosol optical depth (AOD) has become a crucial metric for assessing global
22 climate change. Although global and regional AOD trends have been studied
23 extensively, it remains unclear what factors are driving the inter-decadal variations in
24 regional AOD and how to quantify the relative contribution of each dominant factor.
25 This study used a long-term (1980–2016) aerosol dataset from the Modern-Era
26 Retrospective Analysis for Research and Applications, version 2 (MERRA-2)
27 reanalysis, along with two satellite-based AOD datasets (MODIS/Terra and MISR)
28 from 2001 to 2016, to investigate the long-term trends in global and regional aerosol
29 loading. Statistical models based on emission factors and meteorological parameters
30 were developed to identify the main factors driving the inter-decadal changes of
31 regional AOD and to quantify their contribution. Evaluation of the MERRA-2 AOD
32 with the ground-based measurements of AERONET indicated significant spatial
33 agreement on the global scale ($r = 0.85$, RMSE = 0.12, MFE = 38.7%, FGE = 9.86%,
34 and IOA = 0.94). However, when AOD observations from the China Aerosol Remote
35 Sensing Network (CARSNET) were employed for independent verification, the
36 results showed that MERRA-2 AODs generally underestimated CARSNET AODs in
37 China (RMB = 0.72 and FGE = -34.3%). In general, MERRA-2 was able to
38 quantitatively reproduce the annual and seasonal AOD trends on both regional and
39 global scales, as observed by MODIS/Terra, albeit some differences were found when
40 compared to MISR. Over the 37-year period in this study, significant decreasing
41 trends were observed over Europe and the eastern United States. In contrast, eastern
42 China and South Asia showed AOD increases, but the increasing trend of the former
43 reversed sharply in the most recent decade. The statistical analyses suggested that the
44 meteorological parameters explained a larger proportion of the AOD variability
45 (20.4%–72.8%) over almost all regions of interest (ROIs) during 1980–2014 when
46 compared with emission factors (0%–56%). Further analysis also showed that SO₂
47 was the dominant emission factor, explaining 12.7%–32.6 % of the variation in AOD
48 over anthropogenic aerosol–dominant regions, while BC or OC was the leading factor
49 over the biomass burning–dominant (BBD) regions, contributing 24.0%–27.7% of the
50 variation. Additionally, wind speed was found to be the leading meteorological
51 parameter, explaining 11.8%–30.3% of the variance over the mineral dust–dominant
52 regions, while ambient humidity (including soil moisture and relative humidity) was
53 the top meteorological parameter over the BBD regions, accounting for 11.7%–35.5%
54 of the variation. The results of this study indicate that the variation in meteorological
55 parameters is a key factor in determining the inter-decadal change in regional AOD.

56

57 1. Introduction

58 Atmospheric aerosols play a key role in the energy budget of the Earth's climate
59 system through aerosol–radiation interactions (direct effect) and aerosol–cloud
60 interactions (indirect effect). On the one hand, by absorbing and scattering solar and
61 terrestrial radiation, aerosols generally cool the Earth's surface and heat the atmosphere,

62 depending on the absorption level of the aerosols (McCormick and Ludwig 1967; Ding
63 et al., 2016; Sun et al., 2018; Zheng et al., 2019). This effect is termed the aerosol direct
64 effect. The cooling effect of aerosols may partly counteract the warming caused by the
65 increase in CO₂ and other greenhouse gases in the past several decades (IPCC, 2007).
66 On the other hand, by acting as cloud condensation nuclei or ice nuclei, not only can
67 aerosols alter the microphysical and radiative properties of clouds, as well as their
68 lifetimes (Rosenfeld et al., 2019; Andreae 2009), but they can also change the
69 precipitation efficiency [depending on the aerosol type (Jiang et al., 2018)], modify the
70 characteristics of the atmospheric circulation, and affect the global hydrological cycle
71 (Ramanathan et al., 2001; Ackerman et al., 2000; Hansen et al., 1997; Sarangi et al.,
72 2018). This effect is termed the aerosol indirect effect. Furthermore, depending on their
73 physical and chemical properties, as well as their composition, aerosols can affect
74 ecosystems (Yue et al., 2017; Liu et al., 2017), atmospheric visibility (Che et al., 2007;
75 Wang et al., 2009; Gui et al., 2017; Che et al., 2014), and even human health [such as
76 through their roles in lung cancer, respiratory infection, and cardiovascular disease
77 (Silva et al., 2013; Lelieveld et al., 2015; Cohen et al., 2017)]. Unlike the long-lived
78 greenhouse gases (e.g., CO₂, CH₄ and N₂O), aerosols produced via anthropogenic
79 activity or naturally have relatively short life spans and large spatial and temporal
80 variability. Therefore, it is essential to investigate the long-term variability and
81 inter-decadal trends of atmospheric aerosol loadings on both regional and global scales.

82 Aerosol optical depth (AOD), representing the attenuation of sunlight induced by
83 aerosols and serving as an important measure of aerosol loading, has become a crucial
84 metric in assessing global climate change and the effects of aerosols on radiation,
85 precipitation and clouds. Through the efforts of scientists in various countries over the
86 past three decades, a series of AOD datasets with different time spans derived from
87 continuous ground-based and satellite observations have been accumulated. These
88 datasets have been widely employed to investigate the long-term annual and seasonal
89 trends of AOD at global and regional scales. Although ground-based observations have
90 limited spatial and/or temporal coverage, they can provide more detailed information on
91 aerosol properties and long-term variations for satellite and model validation. For
92 example, using the long-term and high-quality AOD datasets from the Aerosol Robotic
93 Network (AERONET), Li et al. (2014) found that North America and Europe
94 experienced a uniform decrease in AOD from 2000 to 2013. Che et al. (2015) estimated
95 the change in AOD based on AOD data at 12 long-term ground-based sites in China
96 from the China Aerosol Remote Sensing Network (CARSNET) and found that AOD
97 showed a downward trend from 2006 to 2009 and an upward trend from 2009 to 2013.
98 Compared with the spatial sparseness of ground-based observations, inferences from
99 satellite-based sensors can provide a global perspective of AOD change, due to their
100 continuous spatial measurements. Previous studies (Hsu et al., 2012; Pozzer et al., 2015;
101 Mehta et al., 2016; Proestakis et al., 2018; Klingmüller et al., 2016; De Leeuw et al.,
102 2018; Zhang and Reid 2010) have investigated global and regional AOD trends by using
103 multiple satellite observations, including the Moderate Resolution Imaging
104 Spectroradiometer (MODIS), Multiangle Imaging Spectroradiometer (MISR), the
105 Sea-viewing Wide Field-of-view Sensor (SeaWiFS), and others. These studies have

106 shown increased AODs over eastern China, India, the Middle East (ME), and the Bay of
107 Bengal, and decreased AODs over the eastern United States (EUS) and Europe.

108 In general, regional AOD changes are closely linked to the variations in natural
109 emissions driven by meteorological conditions (such as mineral dust) and local
110 anthropogenic emissions associated with economic and population growth. For example,
111 over anthropogenic aerosol–dominant regions, most of the primary pollutant emissions
112 [such as black carbon (BC)] and aerosol precursors (such as SO₂, NO_x and NH₃) in
113 North America and Europe have declined in response to emissions control (Hammer et
114 al., 2018). In contrast, pollutant emissions and their precursors in the rapidly developing
115 countries (such as India and China) have increased over the past few decades,
116 attributable to enhanced industrial activity. However, as a consequence of clean-air
117 actions, anthropogenic emissions in China have declined significantly in recent years
118 (Zheng et al., 2018). It has been proven that these changes in local pollutant emissions or
119 aerosol precursors over the above regions can to a certain extent explain the regional
120 AOD variability, as observed in long-term satellite aerosol data records (Meij et al.,
121 2012; Itahashi et al., 2012; Feng et al., 2018). On the other hand, various studies have
122 shown that meteorological changes play a major role in determining the inter-decadal
123 trend of AOD over mineral dust–dominant regions, particularly in the Sahara Desert (SD)
124 and the ME (Pozzer et al., 2015; Klingmüller et al., 2016). Based on model simulations
125 during 2001–2010, Pozzer et al. (2015) suggested that, over biomass burning–dominant
126 regions, the changes in both meteorology and emissions are equally important for
127 driving AOD trends. Considering the localized changes in anthropogenic aerosol
128 emissions and meteorological conditions in different regions, a key question is whether
129 these factors are responsible for the regional AOD trends, or which main factors
130 dominate the trends. Therefore, it is important to investigate the cause of regional AOD
131 trends in terms of the variations in both anthropogenic emissions and meteorological
132 factors for projecting the response of the Earth-atmosphere system to future changes.

133 In this study, we used a long-term (1980–2016) aerosol dataset obtained from the
134 Modern-Era Retrospective Analysis for Research and Applications, version 2
135 (MERRA-2) reanalysis, along with two satellite-based datasets (MODIS/Terra and
136 MISR) during 2001–2016, to conduct a comprehensive estimation of global and regional
137 AOD trends over different periods. To ensure the reliability of the trend assessment, 468
138 AERONET sites and 37 CARSNET sites with continuous observations for at least one
139 year were used to assess the performance of the MERRA-2 AOD on a global scale.
140 Twelve regions dominated by different aerosol types were selected to explore the
141 relationships between local anthropogenic emissions, meteorological factors, and
142 regional AOD. Furthermore, stepwise multiple linear regression (MLR) models were
143 developed to estimate the regional AOD as a function of emission factors and other
144 meteorological parameters, which allowed the influences of emissions and meteorology
145 to be separated. Then, the Lindeman, Merenda and Gold (LMG) method was applied to
146 the MLR models to identify the main factors driving the regional AOD variability and to
147 quantitatively evaluate the contribution of each driving factor.

148
149

150 **2. Data and methods**

151 **2.1 MERRA-2 aerosol reanalysis data**

152 MERRA-2 is the latest atmospheric reanalysis version for the modern satellite era
153 provided by the NASA Global Modeling and Assimilation Office (Gelaro et al., 2017),
154 using the Goddard Earth Observing System, version 5 (GEOS-5), earth system model
155 (Molod et al., 2012, 2015), which includes atmospheric circulation and composition,
156 ocean circulation and land surface processes, and biogeochemistry. Note that, in
157 MERRA-2, in addition to providing assimilation of traditional meteorological
158 observations, a series of AOD observation datasets, including bias-corrected AODs
159 retrieved from the Advanced Very High Resolution Radiometer (AVHRR) instrument
160 over the oceans (Heidinger et al., 2014) and MODIS (onboard both the Terra and
161 Aqua satellites) (Levy et al., 2010; Remer et al., 2005), and non-bias-corrected AODs
162 retrieved from MISR (Kahn et al., 2005) over bright surfaces and ground-based
163 AERONET observations (Holben et al., 1998), were also assimilated within the
164 GEOS-5 earth system model. An overview of the MERRA-2 modeling system and a
165 more detailed description of aerosols in the MERRA-2 system can be found in Gelaro
166 et al. (2017) and Buchard et al. (2017), respectively. In this study, the three-hourly
167 MERRA-2 analyzed AOD fields, at a resolution of 0.5° latitude by 0.625° longitude,
168 were used for evaluation, while the monthly mean AOD values were used for climate
169 analysis.

170 **2.2 Satellite aerosol data**

171 Two AOD datasets during 2001–2016 retrieved from MODIS and MISR, both
172 onboard the Terra platform, were used in this study. The MODIS sensor onboard the
173 Terra satellite observes the Earth at multiple wavelengths (range: 410–1450 nm; 36
174 bands) with a 2330-km swath, which has provided near-daily global coverage since
175 2000 (King et al., 2003; Levy et al., 2015). This study employed the combined Dark
176 Target/Deep Blue (DTB) AOD algorithm at 550 nm, with a $1^\circ \times 1^\circ$ resolution, from
177 the Level 3 monthly global aerosol dataset for MODIS Terra, Collection 6.1. The
178 average MAE (RMSE) of the Level 3 MODIS/Terra DTB monthly AOD data have
179 been estimated to be about 0.075 (0.120) over land (Wei et al., 2019). Note that
180 MODIS/Aqua L3 was not used because it started late (June 2002). In addition,
181 compared with the linear trend in MODIS/Aqua AOD during the overlapping period
182 (2003–2016), MODIS/Terra AOD shows similar performance worldwide (including
183 spatial-temporal consistency and distribution patterns of trend values) (Fig. S1),
184 although the Terra sensor has been documented to suffer from degradation issues. The
185 similar performance between MODIS/Terra and MODIS/Aqua is mainly attributed to
186 a new calibration approach in the C6 version, which can remove major
187 non-polarimetric calibration trends from the MODIS data (Levy et al., 2013, 2015; De
188 Leeuw et al., 2018).

189 Total column AOD observations from the MISR sensor onboard the Terra
190 satellite, which provides observations of the Earth's atmosphere with nine different

191 along-track viewing zenith angles at four different spectral bands (440–866 nm)
192 (Diner et al., 1998), were utilized. It should be noted that, although MISR has a much
193 narrower swath (~360 km) compared with MODIS, the multi-angle observation from
194 MISR provides the capability for retrieving a more reliable AOD over bright surfaces
195 such as desert areas (Diner et al., 1998; Kahn et al., 2010). The AOD retrieval in the
196 555-nm channel from monthly global aerosol datasets at a spatial resolution of $0.5^\circ \times$
197 0.5° were used in this study. The uncertainty of the MISR Level 2 AOD data over land
198 and ocean has been estimated to be ± 0.05 or $\pm(0.2 \times \text{AOD})$ (Kahn et al., 2005). Note
199 that the wavelength of AOD (555 nm) reported by MISR is different from that of the
200 MERRA-2 and MODIS/Terra datasets (550 nm); however, this slight wavelength
201 difference is not expected to affect our analysis and conclusions regarding AOD
202 annual and seasonal trends.

203 **2.3 Ground-based reference data: AERONET and CARSNET**

204 Owing to the accuracy of ground-based AOD observations, long-term
205 instantaneous AOD observation records from two independent operational
206 networks—AERONET and CARSNET—were used to validate the three-hourly
207 MERRA-2 AOD values. Since there are not enough long-term AERONET
208 observations in China, it was necessary to examine the performance of the MERRA-2
209 analyzed AOD fields using additional AOD observations from CARSNET.
210 CARSNET is a ground-based network for monitoring aerosol optical properties that
211 was first established by the China Meteorological Administration in 2002 (Che et al.,
212 2009). Both AERONET and CARSNET use the same types of sunphotometers, which
213 can observe direct solar and sky radiances at seven wavelengths (typically 340, 380,
214 440, 500, 670, 870 and 1020 nm) within a 1.2° full field of view at intervals of about
215 15 min (Holben et al., 1998; Che et al., 2009). For CARSNET, operating instruments
216 are calibrated and standardized using CARSNET reference instruments, which in turn
217 are regularly calibrated at Izaña, Tenerife, Spain, together with the AERONET
218 program (Che et al., 2009; Che et al., 2018). The cloud-screened AOD [based on the
219 work of Smirnov et al. (2000)] in CARSNET has the same accuracy as AERONET,
220 with an estimated uncertainty of 0.01–0.02 (Eck et al., 1999; Che et al., 2009).

221 In this work, we collected ground-based AOD observations (more than one year
222 of data) from 468 AERONET sites worldwide and 37 CARSNET sites in China. The
223 locations of these ground-based sites are shown in Fig. 1. Detailed information about
224 these AERONET and CARSNET sites is given in Tables S4 and S5. The combined
225 instantaneous AOD data collected by AERONET (quality-assured and cloud-screened
226 Level 2.0 data) during 1993–2016 and CARSNET (cloud-screened Level 2.0 data)
227 during 2002–2014 were used. Moreover, to ensure the reliability of AOD evaluation,
228 the AOD measurements in two adjacent channels (i.e., 440 and 675 nm) from
229 AERONET and CARSNET were subsequently interpolated to 550 nm for MERRA-2,
230 using a second-order polynomial fit to $\ln(\text{AOD})$ vs. $\ln(\text{wavelength})$ (Eck et al.,
231 1999).

232
233

2.4 Emissions inventory and meteorological data

The anthropogenic emissions inventories used in this study were obtained from the Peking University (PKU) website (<http://inventory.pku.edu.cn/>), including total suspended particles (TSP) (Huang et al., 2014), SO₂ (Su et al., 2011), BC (Wang et al., 2014), and organic carbon (OC) (Huang et al., 2015), with a spatial resolution of 0.1° × 0.1° and spanning the period 1980–2014. The emissions were calculated using a bottom-up approach based on fuel consumption and an emissions factor database. Huang et al. (2015) showed that the PKU emissions inventories are broadly similar to those of EDGARv4.2 (Edgar, 2011). Monthly meteorological fields from the MERRA-2 global reanalysis were also utilized, including total surface precipitation, surface wind speed, surface relative humidity (RH), mean sea level pressure, etc. These data have a spatial resolution of 0.5° × 0.625° and span the period 1980–2016 (Gelaro et al., 2017). For more detailed information on the selected meteorological parameters, see Table 1.

2.5 ROIs

In this study, 12 regions of interest (ROIs) dominated by different aerosol types were selected to study the long-term trends in regional aerosol loading and how they are related to local emission changes as well as the variation in meteorological variables. These 12 ROIs included three mineral dust-dominant regions [SD (17°W–20°E, 3°N–25°N), ME (38°E–56°E, 14°N–33°N), and Northwest China (NWC; 73°E–94°E, 35°N–47°N)], three biomass burning-dominant regions [the Amazon Zone (AMZ; 46°W–60°W, 1°S–22°S), Central Africa (CF; 12°E–33°E, 2°S–18°S) and Southeast Asia (SEA; 96°E–127°E, 8°S–18°N)], and six anthropogenic aerosol-dominant regions [EUS (73°W–94°W, 29°N–45°N), western Europe (WEU; 10°W–18°E, 37°N–59°N), South Asia (SA; 72°E–90°E, 10°N–30°N), northern China (NC; 108°E–120°E, 30°N–40°N), southern China (SC; 108°E–120°E, 20°N–30°N) and Northeast Asia (NEA; 125°E–145°E, 30°N–41°N)]. The geographical boundaries of these ROIs are shown in Fig. 1.

2.6 Statistical analysis

2.6.1 Comparison methods

AOD data from the 468 AERONET sites worldwide and the 37 CARSNET sites in China were used to evaluate the performance of the three-hourly AOD datasets from MERRA-2. To ensure the accuracy of the assessment, instantaneous ground-based AOD observations within one hour, obtained from AERONET and CARSNET, were averaged as the hourly mean AOD and compared with those from the MERRA-2 three-hourly AOD datasets (see Fig. 2a for the whole procedure).

The errors and quality of the MERRA-2 AOD retrievals are reported using the (Pearson) correlation coefficient [R, Eq. (1)], the mean absolute error [MAE, Eq. (2)], root-mean-square error [RMSE, Eq. (3)], the relative mean bias [RMB, Eq. (4)], the mean fractional error [MFE, Eq. (5)], the fractional gross error [FGE, Eq. (6)], and the

274 index of agreement [IOA, Eq. (7)] for validating the reanalysis (Yumimoto et al.,
 275 2017).

$$276 \quad R = \frac{\sum_{i=1}^N (O_i - \bar{O})(M_i - \bar{M})}{\sqrt{\sum_{i=1}^N (O_i - \bar{O})^2 \sum_{i=1}^N (M_i - \bar{M})^2}} \quad (1)$$

$$277 \quad MAE = \frac{1}{N} \sum_{i=1}^N |M_i - O_i| \quad (2)$$

$$278 \quad RMSE = \sqrt{\frac{1}{N} \sum_{i=1}^N (M_i - O_i)^2} \quad (3)$$

$$279 \quad RMB = \bar{M} / \bar{O} \quad (4)$$

$$280 \quad MFE = \frac{2}{N} \sum_{i=1}^N \frac{|M_i - O_i|}{M_i + O_i} \times 100 \quad (5)$$

$$281 \quad FGE = \frac{2}{N} \sum_{i=1}^N \frac{M_i - O_i}{M_i + O_i} \times 100 \quad (6)$$

$$282 \quad IOA = 1 - \frac{\sum_{i=1}^N (O_i - M_i)^2}{\sum_{i=1}^N (|O_i - \bar{O}| + |M_i - \bar{M}|)^2} \quad (7)$$

283 Where N is the total number of pairs of modeled (M , i.e. MERRA-2) and
 284 observed (O , i.e. AERONET or CARSNET) values. MFE represents a measure of
 285 overall modeling error without emphasizing outliers. MFE can range from 0 (best
 286 score) to 200%. FGE represents a measure of the estimation bias error that allows
 287 symmetric analysis of over- or underestimation by the model relative to observations.
 288 The maximum and minimum values of FGE are +200 and -200% respectively, and 0
 289 is the best value. IOA represents a standard measure of the degree of model accuracy,
 290 and it ranges from 0 to 1 (perfect agreement) (Willmott, 1981).

291 **2.6.2 Trend analysis and stepwise MLR model**

292 Long-term trend analysis of the AOD from MERRA-2, MODIS/Terra and MISR
 293 was performed, on monthly time series data, using ordinary least-squares linear
 294 regression—a technique widely employed for trend analysis of aerosol data (Hsu et al.,
 295 2012; Pozzer et al., 2015; Klingmüller et al., 2016; Ma et al., 2016; Hammer et al.,
 296 2018). Prior to regression, these data were first deseasonalized by subtracting the
 297 monthly mean for different study periods for each grid cell to eliminate the large
 298 influence of the annual cycle. To better compare the results of the trend analysis, the
 299 MERRA-2 and MISR datasets at high spatial resolution ($0.5^\circ \times 0.625^\circ$ and $0.5^\circ \times 0.5^\circ$,
 300 respectively) were bilinear interpolation to the MODIS/Terra resolution of $1^\circ \times 1^\circ$ (see
 301 Fig. 2b for the whole procedure). Incomplete sampling from the satellite instruments
 302 may introduce biases in long-term trend analysis. Thus, to ensure the reliability of the
 303 trend analysis, each grid cell for the MISR and MODIS/Terra AODs was required to

304 have valid data for at least 60% of the time period before regression was performed.
305 Two-tailed Student's *t*-tests were used to assess the robustness of each trend estimate,
306 and the criterion for statistical significance was set at the 95% confidence level.

307 Pearson's *R* was used to measure the strength of the relationship between AOD,
308 anthropogenic emissions, and meteorological parameters. MLR models of monthly
309 MERRA-2 AODs were built for the 12 ROIs using emission factors, meteorological
310 parameters, and both, as predictors. Four emission factors and 32 meteorological
311 parameters were considered in the MLR models (Table 1). For each ROI, the MLR
312 model could be expressed as

$$y = \beta_0 + \sum_{i=1}^n \beta_i x_i + \varepsilon, \quad (4)$$

313 where *y* is the standardized monthly AOD and (*x*₁ ,..., *x*_{*n*}) is the ensemble of
314 standardized monthly explanatory variables. The standardized regression coefficient
315 β_i was determined by the least-squares method, and ε is an error term.

316 In each step of the MLR model, a variable is considered to be moved or removed
317 from the set of explanatory variables using the stepwise regression method to obtain
318 the best model fit. In other words, for each step the model adds a significant (*P* < 0.05)
319 explanatory variable to the model, it can be removed only if it is insignificant (*P* > 0.1)
320 after adding or removing another variable. A similar model has been widely used to
321 investigate the relationship between aerosols and meteorology (e.g., Yang et al., 2016;
322 Lu et al., 2016; Zhai et al., 2019; Tai et al., 2010).

323 Although the most important explanatory variables were obtained via the above
324 stepwise MLR model, there might be multiple collinearities among different
325 explanatory variables. In that situation, the standardized regression coefficient as an
326 explanation of relative importance is unstable and misleading. To eliminate the
327 influence of multi-collinearity, the variance inflation factor (VIF) (Altland et al., 2006)
328 was used to test whether there was a multi-collinearity problem among the variables.
329 VIF is often regarded as a measure of collinearity between each variable and another
330 variable in the model. VIF can be calculated from the following relationship:

$$\text{VIF} = \frac{1}{1 - R_i^2}, \quad (5)$$

331 where R_i^2 is the coefficient of determination of linear regression between the *i*th
332 independent variable and other independent variables in the model. The present study
333 used a VIF threshold of 10, which is widely recommended in the literature (e.g., Hair
334 et al., 2010; Barnett et al., 2006; Field, 2005), to represent the maximum acceptability
335 of collinearity.

336 Finally, to better quantify the relative contributions of each independent
337 explanatory variable, which were obtained from the stepwise MLR model, to AOD
338 variability, the LMG method (Bi 2012; Grömping 2006; Lindeman et al., 2014) was
339 applied. This approach is one of the most advanced methods for determining the
340 relative importance of explanatory variables in a linear model and provides a
341 decomposition of the fraction of model-explained contributions (i.e., R^2) into

342 nonnegative contributions using semi-partial R values. The LMG measure for the i th
343 regressor x_i can be expressed as

$$\text{LMG}(x_i) = \frac{1}{p!} \sum_{r \text{ permutation}} \text{seq}R^2(\{x_i\}|r), \quad (6)$$

344 where r represents the r th permutation ($r = 1, 2, \dots, p!$), and $\text{seq}R^2(\{x_i\}|r)$ represents
345 the sequential sum of squares for the regressor x_i in the ordering of the regressors in
346 the r th permutation.

347 For a detailed introduction to and description of the calculation process of the
348 LMG measure, refer to Grömping (2006). For all variables (including the AODs from
349 MERRA-2, MISR and MODIS/Terra, the meteorological variables from MERRA-2,
350 and the emission estimates from PKU), the regional mean was calculated by
351 averaging valid variable values over all grids within the twelve ROIs. For the seasonal
352 analysis, the four seasons were considered as follows: spring (March–April–May),
353 summer (June–July–August), autumn (September–October–November), and winter
354 (December–January–February).

355 **3 Results and discussion**

356 **3.1 Assessing the performance of the MERRA-2 AOD datasets** 357 **on the global scale**

358 Although the official documentation points out that a large number of AOD
359 observations have been assimilated into the system (Buchard et al., 2017), the global
360 performance of MERRA-2 AOD is still unknown. In addition, since MERRA-2
361 assimilates a variety of AOD datasets from different observation periods (such as
362 AVHRR before 1999, AERONET since 1999, and EOS-era satellite after 2000)
363 (Buchard et al., 2017), it is difficult to disentangle the influence of each assimilated
364 dataset alone on the overall accuracy of MERRA-2. Strictly speaking, we need to
365 point out that MERRA-2 and AERONET are not independent of each other (after
366 1999). Nevertheless, we hope that this assessment will still provide some reference for
367 other studies using the MERRA-2 AOD dataset. Therefore, we first use AERONET to
368 evaluate the overall performance of MERRA-2 AOD on the global scale, and then use
369 CARSNET to independently examine the performance of the MERRA-2 analyzed
370 AOD field in China.

371 **3.1.1 MERRA-2 versus AERONET**

372 Using all of the collected AERONET observations, the overall performance of the
373 MERRA-2 AOD on a global scale was validated first. The results showed significant
374 spatial agreement between MERRA-2 and ground-based AOD on the global scale,
375 with an acceptable bias ($r = 0.85$, RMSE = 0.12, MAE = 0.06, and MFE=38.73%)
376 (Fig. 3a). Moreover, Fig. 4 shows site-to-site comparisons of the three-hourly
377 MERRA-2 AOD at 550 nm and the collocated AERONET AOD observations, and a
378 statistical summary of the comparison and the location information for each site are
379 given in Table S4. Globally, the MERRA-2 AOD datasets exhibited high R values
380 against ground-based observations: over 83.3%, 59.0% and 28.0% of sites had an R
381 greater than 0.6, 0.7 and 0.8, respectively; 95.9% and 87.6% of sites had an IOA
382 greater than 0.8 and 0.9, respectively; 85.3 % and 50.4% of sites had an MAE lower
383 than 0.1 and 0.05, respectively; 22.6% and 59.8% of sites had an MFE lower than 30%
384 and 40%, respectively; and more than 69.9% and 89.3% of sites had an RMSE less
385 than 0.1 and 0.2, respectively. These results indicated that, although MERRA-2 does
386 not perform well in some individual regions, it does not affect the global accuracy of
387 MERRA-2 as the latest global aerosol reanalysis dataset, especially in comparison
388 with other satellite datasets. In addition, the obvious regional differences in the global
389 performance of MERRA-2 AOD should not be overlooked. According to Figs. 4c and
390 e, the RMB was greater than 1 and FGE was greater than 0% in the United States,
391 southern South America and Australia, which indicates that MERRA-2 overestimates
392 the AOD in these regions. This overestimation may be attributed to the bias of MISR
393 AOD in these areas (not shown here) and the fact that AERONET was not assimilated
394 in MERRA-2 until 1999 (Buchard et al., 2017). In contrast, there clear

395 underestimation was found in other regions, such as the Amazon Basin, southern
396 Europe, SA, and SEA. This apparent underestimation (FGE = -23.9%, see Fig. S2b)
397 in NC was further confirmed using additional ground-based AOD observations from
398 CARSNET (reported in the following section). Notably, this underestimation seems to
399 be systematic, as negative RMB and FGE were found in most parts of the Northern
400 Hemisphere, except the United States. Such systematic underestimation over these
401 regions is likely due to the lack of nitrate aerosols in the GOCART model (Buchard et
402 al., 2017). Furthermore, the underestimation seems to be more prominent in high
403 nitrate-emissions areas such as NC and SA.

404 To ensure the accuracy of inter-annual variations of AODs over different ROIs (as
405 defined in Fig. 1), the regional performance of MERRA-2 AOD was evaluated by
406 integrating all sites within each ROI (Table 2 and Figs. S2). Regionally, R ranged
407 from 0.7 to 0.95 among the 12 ROIs, with the highest R (0.95) occurring in the ME
408 and the lowest (0.7) in the EUS. Similar to the site-to-site FGE distribution, the FGE
409 presented a systematic overestimation in the EUS of around 17.82%. In contrast, the
410 FGE showed significant systematic underestimation in NC, SA, CF and SEA, with the
411 degree of underestimation being 23.9%, 8.1%, 23.0% and 8.5%, respectively.
412 Significant differences in these regions were also supported by small RMBs of 0.71,
413 0.87, 0.75 and 0.84, respectively.

414 The MERRA-2 AOD datasets performed better over SA than over NC, which is
415 one of the most polluted areas in the world, in terms of a smaller MAE (0.11) and
416 RMSE (0.18) (Fig. S2f). The better performance over SA is likely due to more AOD
417 observations having been assimilated in MERRA-2 compared to over NC (Buchard et
418 al., 2017). For NEA, SC and WEU, MERRA-2 AOD generally compared well to
419 AERONET AOD, with the MAE being less than 0.1, MFE less than 35%, and RMB
420 greater than 0.93. For the SD, results were relatively poor in that the MAE was greater
421 than 0.1 and the RMSE greater than 0.2. Besides, although MERRA-2 performed well
422 in NWC when only one AERONET site was used, after using additional CARSNET
423 ground-based observations it was found that the MERRA-2 AOD performance in
424 NWC needs to be improved (Fig. S3c). Notably, MERRA-2 was found to produce
425 lower AOD than AERONET, and the bias between them was more obvious for high
426 AERONET AODs. For instance, the MERRA-2 AODs over most polluted areas (such
427 as the anthropogenic aerosol-dominant regions of NC and SA and the biomass
428 burning-dominant regions of SEA and South America) were almost always lower
429 than those of AERONET when the AERONET AOD was greater than 1.5. This
430 indicated that MERRA-2 does not capture all high-AOD events well (such as serious
431 haze events over NC and SA, and frequent biomass burning events over SEA), due to
432 the following three reasons: (1) a relatively low quantity of ground-based-observed
433 aerosol data can be used for assimilation; (2) the MERRA-2 system model lacks an
434 adequate source of anthropogenic emissions with high temporal resolution; and (3) a
435 lack of nitrate aerosols in the GOCART model (Chin et al., 2002; Colarco et al., 2010;
436 Buchard et al., 2017).

437 **3.1.2 MERRA-2 versus CARSNET**

438 Since CARSNET is not assimilated in MERRA-2, it is considered for
439 independent verification. Using all of the collected CARSNET observations, the
440 performance of the MERRA-2 AOD in China was validated. Statistical measures for
441 MERRA-2 AOD at each CARSNET site are shown in Fig. 4 and Table S5, and those
442 for regional performance (i.e. NEC, NC and SC) are shown in Table 2 and Fig. S3. In
443 general, the comparison results using CARSNET as reference showed that the
444 performance of MERRA-2 AOD in China ($r = 0.70$, RMSE = 0.33, MAE = 0.22, and
445 MFE = 46.63%) is much worse than that of MERRA-2 AOD on a global scale (Fig.
446 3a). Regionally, compared with the results from using three AERONET sites as a
447 comparison, the results comparing CARSNET and MERRA-2 AOD showed a similar
448 pattern—that is, the underestimation of MERRA-2 AOD over NC is universal.
449 MERRA-2 underestimated the AOD at almost all CARSNET sites (Fig. 4e and Table
450 S5), with an overall MAE of 0.23, RMSE of 0.33, MFE of 47.3%, and
451 underestimation of ~35.5% (Fig. S3a). Similar results based on CARSNET
452 observations in China have also been reported in the literature (Song et al., 2018; Qin
453 et al., 2018). Specifically, there was higher agreement over SC compared with NC
454 (Fig. S3b), mainly because nitrate aerosols in China are mainly concentrated in
455 industrially intensive areas such as Henan, Shandong, Hebei, and the Sichuan Basin
456 (Zhang et al., 2012). The lack of a nitrate module in the GOCART model will cause
457 further AOD uncertainty in these above areas, which is the main reason behind the
458 relatively low performance of MERRA-2 AOD in these areas.

459 The purpose of this work was to study the inter-annual or inter-decadal variations
460 of AOD in different regions. Therefore, taking MODIS/Terra and MISR AOD as a
461 reference, the accuracy of MERRA-2 annual-mean AOD was evaluated at global and
462 regional scales (Figs. S4 and S5). Globally, the overall spatial correlations between
463 the MERRA-2 AOD and MODIS/Terra and MISR AOD datasets was found to be
464 quite acceptable, with no apparent disagreements in the annual AOD variations during
465 2001–2016 (Fig. S5). Besides, although an offset was found between MERRA-2,
466 MODIS/Terra and MISR in terms of absolute values of AOD in some ROIs, the
467 short-term tendency during the overlapping period was similar among the three
468 datasets (Fig. S4). Because the aerosol retrieval algorithm based on satellite
469 observation does not work well under cloudy conditions or for bright surfaces, there
470 are always numerous missing values in satellite-retrieved AOD datasets. In contrast,
471 not only is the accuracy of the MERRA-2 AOD dataset comparable with satellite
472 observations (Fig. S4), it also provides a complete AOD record from 1980 to the
473 present day. These reasons give confidence that the MERRA-2 aerosol dataset is
474 suitable for analysis of the variations in AOD. Thus, the AOD values from
475 MERRA-2's aerosol analysis fields, in combination with the AOD datasets derived
476 from two satellite sensors, were used to comprehensively analyze the spatiotemporal
477 variability of aerosols at global and regional scales.

478 **3.2 Global AOD distribution and inter-annual evolution of** 479 **regional AOD**

480 Figure S6 shows the global annual- and seasonal-mean AOD distribution
481 calculated from the MERRA-2 AOD products during 1980–2016. Furthermore, the
482 distributional characteristics of the global annual-mean AOD from MERRA-2,
483 MODIS and MISR during the same period (2001–2016) are also compared in the
484 figure. The comparison shows that, although MISR underestimated the AOD (e.g., in
485 SA and eastern China), as expected because of insufficient sampling (Mehta et al.,
486 2016; Kahn et al., 2009), the three AOD products were generally closely consistent on
487 the global scale (also see Fig. S5). Generally, high AOD loading was mainly observed
488 in areas of high anthropogenic and industrial emissions, such as in eastern China and
489 India, and major source areas of natural mineral dust—particularly the Saharan,
490 Arabian and Taklimakan deserts.

491 Due to the seasonal variation of the atmospheric circulation driven by solar
492 radiation and the intensity of human activities in different regions, the global
493 distribution of AOD also shows obvious seasonal differences, with global aerosol
494 loading reaching its maximum in spring and summer. On the one hand, this can
495 mainly be attributed to the enhanced circulation in spring and summer, which
496 increases the likelihood of natural mineral dust from several major dust sources in the
497 Northern Hemisphere (i.e., the Sahara and Sahel, the Arabian Peninsula, Central Asia,
498 and the Taklimakan and Gobi deserts) being brought into the atmosphere; plus, along
499 the westerly belt, airflow dust can be transmitted to surrounding sea areas (such as the
500 strip of the northern tropical Atlantic stretching between West Africa and the
501 Caribbean, the Arabian Sea, and the Bay of Bengal) and more remote
502 areas (such as South America, the Indo-Gangetic Plain, and the eastern coastal areas
503 of China, Korea, and Japan) (Mao et al., 2014). On the other hand, higher
504 temperatures and damp air in summer can create favorable conditions for the
505 hygroscopic growth and secondary formation of aerosols (Minguillón et al., 2015;
506 Zhao et al., 2018), which raises the AOD in some areas, such as NC and northern
507 India, dominated by anthropogenic aerosol emissions in summer. Moreover, frequent
508 local biomass-burning aerosol emissions in central Africa during summer is the main
509 cause of high AOD in the region (Tummon et al., 2010).

510 In contrast, global aerosol loading is relatively low in autumn and winter. The
511 atmosphere in autumn and winter is generally more stable and vertical mixing is
512 weaker, and thus it is difficult for more aerosols—particularly natural mineral
513 dust—to be brought into the atmosphere, which leads to lower AOD in autumn and
514 winter (Zhao et al., 2018). Nevertheless, the AOD in autumn in South America, SEA,
515 SC and CF is clearly high, which is mainly attributable to the emission of large
516 amounts of fine aerosol particles (i.e., BC and OC) from frequent biomass burning in
517 these regions (Thornhill et al., 2018; Ikemori et al., 2018; Chen et al., 2017). Notably,
518 fine particulate matter composed of sulfate–nitrate–ammonium aerosols, which is
519 produced by high-intensity anthropogenic activities in autumn and winter, is still the
520 main contributor to high AOD in eastern China and India (Gao et al., 2018; David et
521 al., 2018).

522 To better characterize the temporal evolution of regional AOD, the monthly mean
523 AODs over the 12 ROIs from 1980 to 2016 were calculated. As illustrated in Fig. 5,

524 the monthly regional AOD had large seasonal variability, in addition to varying
525 degrees of fluctuation in different periods. In areas dominated by smoke aerosols from
526 biomass burning (i.e., AMZ, CF and SEA), biomass-burning events tend to occur in
527 the warm season (May to October), leading to a more prominent monthly AOD at this
528 time of the year compared with the cold season (November to April). It is noteworthy
529 that MERRA-2 also captured several well-known forest-fire events, such as those in
530 Indonesia in 1983 and 1997, which have been proven to be mainly related to climatic
531 drying caused by El Niño and large-scale deforestation (Page et al., 2002; Goldammer
532 2007). In the CF region, the monthly mean maximum AOD experienced a
533 transformation process—that is, the monthly maximum AOD often occurred in June
534 and July before 2000, whereas after 2000 it occurred more frequently in August and
535 September. This shift may be attributed to the fact that MERRA-2 did not assimilate
536 any land-based AOD observations before 1999, which made it difficult for the model
537 to simulate the monthly variation of regional AOD (Gelaro et al., 2017; Buchard et al.,
538 2017). In the AMZ and SEA regions, September and October seems to be the two
539 most frequent months for the occurrence of high AOD values, but the magnitude of
540 AOD values has decreased in recent years, which may be related to changes in
541 meteorological conditions (Torres et al., 2010).

542 In areas dominated by natural mineral dust aerosol (i.e., the SD, ME and NWC),
543 the monthly maximum AOD mainly occurred in March–August. Before 2000, there
544 were many anomalies of the AOD monthly maximum, which also implied frequent
545 sandstorms. In contrast, the frequency of monthly AOD anomalies decreased after
546 2000, which may be attributable to the reduced surface wind speed and increased
547 vegetation cover (Kim et al., 2017; Wang et al., 2018; An et al., 2018). Compared
548 with the areas dominated by smoke and dust aerosols, the seasonal differences of
549 AOD in the areas dominated by anthropogenic aerosol emissions appear to be smaller,
550 but their temporal evolution is more pronounced. In NEA, the monthly maximum
551 AOD often occurred in March–June, possibly related to the long-distance
552 transportation of sand and dust in the China–Mongolia deserts (Taklimakan and Gobi).
553 However, as the frequency of sandstorms has decreased in the past 10 years (An et al.,
554 2018), the monthly maximum AOD has also shown a downward trend. In NC and SA,
555 the monthly AOD has gradually expanded outward since 1980, indicating that AOD
556 has experienced a gradual increase. Monthly AOD had large seasonal variability in
557 the SC region, reaching its maximum in February–April. The increased aerosol
558 emissions from biomass burning in spring seem to be one of the main reasons for high
559 AOD in the SC region (Chen et al., 2017). For the EUS and WEU regions, the
560 characteristics of the monthly variation in AOD were similar—that is, large values of
561 AOD occurred in summer. With time, the monthly AOD showed a tendency to
562 gradually shrink inwards, suggesting AOD has experienced a significant decline over
563 the past few decades in the EUS and WEU. The main drivers of the inter-annual
564 variability of AOD over each ROI are discussed in detail in sections 3.5 and 3.6.

565 **3.3 Global AOD trend maps**

566 Annual and seasonal linear trends of the MERRA-2 AOD anomaly were

567 separately calculated for each $1^\circ \times 1^\circ$ grid cell for the whole of 1980–2016 period
568 (period 1) and for the first 18 years (1980–1997, period 2) and last 19 years (1998–
569 2016, period 3). Figure 6 shows the spatial distribution of these trends on the global
570 scale. Throughout period 1, the regions where annual AOD showed a significant
571 upward trend ($p < 0.05$) were mainly located in eastern China, SA, the ME, northern
572 South America, and the southern coastal areas of Africa, whereas some significant
573 downward trends were observed in the whole of Europe and the EUS. However,
574 compared with the annual trends, the seasonal AOD trends had obvious regional
575 differences in terms of their spatial distribution. For instance, a strong positive trend
576 throughout East Asia, including Korea and Japan, was found in spring. In summer,
577 there was a significant upward and downward AOD trend in north-central Russia and
578 the Amazon basin, respectively. In contrast, winter AOD had a significant downward
579 trend in the area north of 40°N . These differences in seasonal trends are closely
580 related to the seasonal variations in anthropogenic aerosols generated by local
581 emissions and natural aerosols driven by meteorological conditions (De Meij et al.,
582 2012; Chin et al., 2014).

583 In the two different historical periods (i.e., period 2 and 3), these trends seem to
584 have experienced a remarkable shift. During period 2, the annual AOD had a
585 significant upward trend throughout the Southern Hemisphere, and similar upward
586 trends also existed in eastern and northwestern China. This upward trend in the
587 Southern Hemisphere, which was most likely associated with two giant volcano
588 eruption events in the early 1980s [El Chichón (Hofmann and Rosen 1983)] and early
589 1990s [Pinatubo volcanoes (Stenchikov et al., 1998; Bluth et al., 1992; Kirchner et al.,
590 1999)], is also reflected in the regional annual mean AOD time series shown in Fig.
591 S4. The eruptions led to a strong increase in volcanic ash and SO_2 emissions,
592 consequently increasing AODs from place to place via airflow transport, which was
593 captured accurately by MERRA-2. Meanwhile, AOD had a significant downward
594 trend throughout Europe and the EUS, which appears to be related to the reduction of
595 TSP and SO_2 emissions (see section 3.5). Seasonally, a significant upward trend
596 seems to be prevalent in all seasons in the Southern Hemisphere. Compared with
597 other seasons, the decline of AOD was more obvious in Europe and America. In
598 winter, except for the positive trend that still existed in the marine area of the
599 Southern Hemisphere, the fluctuations in other regions were smaller and relatively
600 stable.

601 During period 3, AOD began to show a significant upward trend in most regions,
602 especially in SA, SEA, the ME, central Russia, the western United States, and
603 northern South America, whilst still maintaining an upward trend in eastern China
604 with greater intensity. These upward trends over SA, the ME and eastern China are in
605 good agreement with the results of Hsu et al., (2012), who used SeaWiFS AOD
606 records from 1997 to 2010. It is worth noting that the trends for the whole of Europe
607 shifted from significantly positive to statistically insignificant, while the region that
608 had shown a significant downward trend before 1997 in the EUS was also shrinking.
609 Furthermore, the region showing a positive trend, prevailing in the Southern
610 Hemisphere, shrunk dramatically. Similarly, the spatial distribution of the trend also

611 had significant differences in different seasons of this period. In spring and winter,
612 only significant upward trends could be observed on a global scale, mainly in eastern
613 China, SA, the ME and South America. Conversely, significant downward trends
614 were apparent in the EUS, Northwest Africa and central South America in summer.
615 Additionally, it was also found that the region with a significant downward trend in
616 Africa shifted from the northwest in summer to the southwest in autumn. The joint
617 effect of the changes in local emissions and meteorological conditions determined
618 these trends in these regions. See Section 3.5 for a more detailed explanation.

619 Ensuring the accuracy of AOD trends calculated by MERRA-2 is critical for
620 quantifying the contribution of local emissions and meteorological factors to the
621 inter-decadal variation of AOD in different regions. For comparison, the resulting
622 annual and seasonal trends of the MERRA-2, MODIS/Terra, and MISR AOD
623 anomaly over the whole globe were derived, using the same method, between 2001
624 and 2016; the results are shown in Fig. 7. This comparison shows that the AOD trends
625 during 2001–2016 calculated by MERRA-2 in most regions of the world agreed well
626 with the results of MODIS and MISR, on both annual and seasonal timescales.
627 Although MERRA-2 assimilates MODIS and MISR at the same time, the relatively
628 small difference between MERRA-2 and MISR may be mainly due to the insufficient
629 sample size of MISR (MODIS produces three to four times more data than MISR)
630 (De Meij et al., 2012).

631 For the annual trend, the significant upward trend observed by MODIS/Terra and
632 MISR in SA and the ME and the significant downward trend observed in the EUS,
633 WEU and central South America were consistent with the results of the MERRA-2
634 trend. Similar trends were reported in a previous study based upon 14 years (2001–
635 2014) of observational records (Mehta et al., 2016). Similarly, upward trends also
636 existed in spring, autumn and winter, while downward trends were also apparent in
637 spring, summer and autumn. It should be noted that the trend signals calculated from
638 MERRA-2 and MODIS/Terra were opposite in SC. The difference in sign associated
639 with trends during 2001–2016 could mainly be due to the larger deviation between
640 MERRA-2 and MODIS/Terra between 2001 and 2004 (Fig. S4c). The large deviation
641 directly led to a reversal of trend throughout the period 2001–2016. This deviation
642 may be related to the use of different versions of MODIS data: in the MERRA-2 AOD
643 observing system, MERRA-2 assimilated the bias-corrected AOD derived from
644 MODIS radiances, Collection 5 (Buchard et al., 2017), and the MODIS data used in
645 this study was the latest collection (Collection 6.1). Different versions mean
646 differences in algorithms (Fan et al., 2017), which may affect the statistical error.

647 **3.4 Regional AOD trends**

648 To examine the spatial and temporal changes in more detail, the annual trend over
649 the globe and in the 12 ROIs, derived based upon MERRA-2 during periods 1, 2 and
650 3, were calculated. In addition, for comparison purposes, the regional trends in AODs
651 from MERRA-2, MODIS and MISR during 2001–2016 were also estimated. It should
652 be noted that different data sets may have a certain effect on global and regional trend
653 assessment due to their own uncertainties. Nevertheless, we include them for

654 completeness but exercise with caution when interpreting the differences in trend
655 values between different data sets. The comparisons of the magnitudes of global
656 annual trends with these regional trends are summarized in Fig. 8 and Table S1. In
657 general, the annual trends derived from different datasets were small on the global
658 scale. As indicated by the results in Fig. 8 and Table S1, the trend values were
659 -0.00068 yr^{-1} for the globe during period 1, with statistical significance at the 95%
660 confidence level. In contrast, no statistically significant trend was detected at the
661 global scale for period 2 (0.00050 yr^{-1}) or 3 (0.00038 yr^{-1}). Analyzing the global
662 AOD trends during 2001–2016 from MERRA-2 and the two satellite datasets, it was
663 found that the MERRA-2 trends were negligible, whereas significant positive
664 (negative) trends were found for MODIS (MISR).

665 However, the trends could be considerable on regional scales. For example, over
666 the anthropogenic aerosol-dominant regions for periods 1, 2 and 3, strong positive
667 trends were apparent over NEA, NC, SC and SA, while strong and statistically
668 significant negative trends were found over WEU and EUS. For biomass-burning
669 regions (SEA, CF and AMZ, but not CF, which had a negligible and insignificant
670 trend), there was a positive trend during periods 1, 2 and 3. For the mineral dust-
671 dominant regions, although there seemed to be an upward trend over the ME, the
672 estimated trends were not statistically significant for other areas, such as NWC and
673 the SD. During 2001–2016, the estimated MERRA-2 AOD trend in most ROIs (i.e.,
674 NEA, SA, ME, WEU, EUS, and AMZ) was comparable to and had the same sign as
675 the trend from both the MODIS and MISR sensors. However, it was opposite in sign
676 to the MISR data over NC, NWC and the SD, and to the MODIS data over SC, SEA
677 and CF during overlapping years. These differences in global trends between
678 MERRA-2 and satellite may be related to several aspects, including the difference in
679 sample number, data accuracy, different measurement methods, etc. (De Meij et al.,
680 2012).

681 In addition to the annual trend, the seasonal trend of AOD for different datasets in
682 different ROIs and different historical periods was also studied (Fig. S7 and Table S1).
683 Globally, negative trends were observed throughout the four seasons during period 1,
684 especially during summer, autumn and winter (-0.00078 , -0.00092 and -0.00097 yr^{-1} ,
685 respectively; statistically significant at the 95% confidence level). On the contrary,
686 there was a negative trend in period 2, although it was not significant. In the
687 subsequent period, period 3, the trend values shifted from negative to positive. The
688 positive trend was more significant in spring and autumn (0.00053 and 0.00070 yr^{-1}).
689 Regionally, strong positive trends were apparent over both NC and SC throughout the
690 four seasons during periods 1, 2 and 3. Strong upward trends were also found over SA.
691 These upward trends were most likely associated with an increase in urban/industrial
692 pollution in China and India. Meanwhile, some similar but relatively moderate
693 upward trends also existed over NEA in spring. In contrast, strong negative trends
694 were observed over the WEU and EUS regions, especially during spring, summer and
695 autumn. The negative trends over WEU and the EUS may partly have been due to a
696 decrease in polluting aerosols associated with emission control measures (De Meij et
697 al., 2012; Li et al., 2014). A statistically significant upward trend was also found over

698 the SD, NWC and the ME in spring during periods 1, 2 and 3 (0.00252, 0.00300 and
699 0.00463 yr⁻¹), respectively. In contrast to the strong downward trends over AMZ in
700 summer during periods 1, 2 and 3, there appeared to be upward trends in spring over
701 AMZ and in winter over CF and AMZ. When compared with the regional trends
702 during 2001–2016 calculated by the two satellite datasets, we found that the seasonal
703 trends of MERRA-2 were highly consistent with the satellite results in almost all
704 regions, especially in spring and autumn. It is worth noting that the trend differences
705 among the three different datasets in all four seasons still existed in NC and SC, and
706 the differences had different seasonal characteristics. For example, over NC, the most
707 significant difference occurred in spring and summer, whereas it occurred in summer
708 and winter over SC. Seasonal differences in trends are mainly due to insufficient
709 accuracy of MERRA-2 in China (see Section 3.1.2).

710 Since the sign of a trend value often varies with the span of the calculation period,
711 it was necessary to evaluate the sliding trend of different periods to help examine the
712 time node of the changes more precisely. Therefore, sliding trend analyses were used
713 to present a more comprehensive analysis of annual trends over the 12 ROIs during
714 different historical periods (Fig. 9). These trends were calculated for all periods
715 starting each year from 1980 to 2007 and ending in 2016 with increments of at least
716 10 years. As shown in Fig. 9, in the EUS and WEU, the AOD experienced a large
717 decline up until the 1981–1990 period, and then the trend reversed moderately from
718 1984 to 1986, declined sharply from 1989 after a short increase from 1996 to 1999,
719 and then sustained a moderate downward trend in the last 17 years. A similar pattern
720 was found for NWC, SD and AMZ, although there was a stronger upward trend and
721 relatively weaker downward trend in the corresponding period. In SC and NC, the
722 AOD experienced a slight increase in the 1980s and a short-term decline around the
723 1990s, and then showed its largest positive trend since 1995 before reversing sharply
724 in the last 10 years (Sun et al., 2019). A similar evolution also existed in NEA and the
725 ME, although the intensities of the trends were relatively weak. In addition to the
726 negligible downward trend in the 1980s and 1990s, SA showed overall positive trends
727 throughout the period, corresponding to increasing anthropogenic emissions (Figure
728 11). Furthermore, in CF, a moderate increasing trend was detected from 1983 to 1985;
729 then in 1990, and the trends became relatively stable but unexpectedly showed sharp
730 increases after 1993, followed by a significant decline in the 2000s and reversal in the
731 last 10 years. The trends for SEA were much smaller and relatively stable. Also, note
732 that around 1985 and 1990 two distinct opposite trend signs were found in all regions.
733 These two unexpected trends indicated that large volcanic eruptions not only greatly
734 affect short-term changes in local aerosols, but also impose different degrees of
735 disturbance in long-term trends of aerosols in different regions of the world (Hofmann
736 and Rosen 1983; Stenchikov et al., 1998; Kirchner et al., 1999)..

737 Furthermore, considering that aerosol concentration and composition usually
738 have strong seasonal cycles (Li et al., 2018), the trends for each season were also
739 calculated separately and compared with the MODIS and MISR trends in the period
740 of overlap (2001–2016). Note that Fig. 10 only shows the evolution of seasonal and
741 annual trends for every 10-year period starting from 1980 to 2007 for MERRA-2, and

742 from 2001 to 2007 for MODIS and MISR; refer to Figs. S8–11 for a fuller
743 presentation of the regional seasonal trend. For all regions, the trends for all seasons,
744 except autumn in SEA, CF and AMZ and spring in the SD, were in phase with the
745 annual trend (also see Fig. S12). In general, autumn trends over SEA, CF and AMZ
746 were larger and often out of phase, possibly attributable to the sudden increase in
747 aerosol concentration caused by biomass-burning events. Similarly, the spring trend
748 over the SD was also larger and more asynchronous than in other seasons. This
749 phenomenon can mainly be attributed to active spring dust events (Liu et al., 2001). In
750 addition, compared with the annual and seasonal regional trends during 2001–2016
751 (Fig. 8 and Fig. S7), the decadal trends of MERRA-2 agreed better with the trend
752 results from MODIS and MISR. This implies that the trends can change relatively
753 quickly with time (Li et al., 2018). Supporting evidence was also found from the
754 strongest trends on both annual and seasonal scales being mostly concentrated in the
755 lower *y*-axis values (Fig. 9 and Figs. S8–11). These results also highlight the
756 importance of evaluating temporal shifts or decadal AOD trends.

757 **3.5 Response of inter-decadal variation in regional AOD to local** 758 **emissions and meteorological parameters**

759 Previous studies have shown that the inter-annual variations in regional AOD are
760 mainly controlled by changes in emissions and meteorological factors (De Meij et al.,
761 2012; Pozzer et al., 2015; Itahashi et al., 2012; Zhao et al., 2017; Lee et al., 2016;
762 Chin et al., 2014). First, the trends of the four emission factors (i.e., TSP, SO₂, BC,
763 and OC) and their correlations with AOD were calculated for the whole study period
764 (1980–2014), as well as for two individual periods (i.e., 1980–1997 and 1998–2014).
765 Note that the PKU global emissions inventories were only available for 1980–2014,
766 which limited our research to a relatively short period. Figures 11 and S13 show the
767 linear trends in emissions and their relationships with MERRA-2 AOD during 1980–
768 2014, respectively. The decreasing AOD trends over Europe and the EUS (see Fig. 6)
769 coincided with substantial reductions in the emissions of primary anthropogenic
770 aerosols (TSP and BC) and precursor gases (SO₂), corresponding to pollution controls
771 (Hammer et al., 2018; De Meij et al., 2012). This was also supported by significant
772 positive correlation between AOD and emissions in most regions of Europe and the
773 EUS (Fig. S13).

774 Positive trends in TSP and SO₂ were present over India and eastern China, which
775 explained the significant upward trend of AOD in these two regions. In addition,
776 eastern China and India experienced a shift in the emissions trend during the two
777 periods (Figs. S14 and 16). In 1980–1997, a significant upward trend existed in both
778 regions (Huang et al., 2014). In contrast, in 1998–2014, India at least maintained this
779 upward trend for all four emission factors, with it sometimes being even stronger,
780 while the positive trends in emissions of TSP and SO₂ over eastern China were
781 interspersed with negative trends. More importantly, the trend of BC and OC in
782 eastern China reversed completely. The shift in these emission trends in eastern China
783 can mainly be attributed to the implementation of multiple emission reduction policies

784 (Zheng et al., 2018). The reductions in emissions were at least partly responsible for
785 the decreasing trend of AOD in the NC and SC regions in the last 10 years (see Fig. 9).
786 The trends in primary BC emissions followed a similar pattern as the trends in OC
787 emissions, except there were positive trends over northeastern China and the positive
788 (negative) trends over CF, AMZ and SEA (WEU and SC) were lower in magnitude,
789 reflecting regional changes in fire activity. There were positive AOD trends in areas
790 dominated by biomass burning (especially in CF and SEA), in response to increased
791 BC and OC emissions. Because human activities are scarce in desert areas, there was
792 no direct relationship between AOD and emissions, as expected. Therefore, this
793 highlights the importance of studying how natural factors (here, this refers to
794 meteorological parameters) control the inter-annual variation of AOD in different
795 desert areas. Furthermore, it is worth noting that in the two short periods (especially
796 1998–2014), these regions with significant positive correlation shrunk and were no
797 longer significant (Figs. S15 and 17), suggesting other factors such as meteorological
798 parameters might be driving the inter-annual trend of regional AOD.

799 To investigate the roles of meteorological parameters in the decadal variation of
800 AOD, Pearson's R values between AOD and meteorological parameters (a total of 32;
801 see Table 1) and over the 12 ROIs for the three periods (i.e., 1980–2014, 1980–1997
802 and 1998–2014) were calculated. Some of these meteorological variables, such as
803 surface precipitation, surface wind speed, wind velocity, RH, and surface wetness,
804 have been shown before to be correlated with regional AOD (Klingmüller et al., 2016;
805 Pozzer et al., 2015; Chin et al., 2014; He et al., 2016). Correlation analysis showed
806 similar correlation patterns between AOD and meteorological parameters for the three
807 different periods over all ROIs. During the period 1998–2014, the correlation was
808 generally stronger than in the other two periods (see Fig. S18), suggesting
809 meteorological factors may have played a more important role in this period. In
810 addition, these correlations seemed to be similar in regions dominated by the same
811 aerosol type. For example, in the mineral dust-dominated regions (i.e., NWC, ME and
812 the SD), AOD had a significant positive (negative) correlation with near-surface wind
813 speed (soil moisture), suggesting that surface wind speed and soil moisture may be the
814 main factors controlling the dust cycle, which is consistent with previous studies in
815 the ME (Klingmüller et al., 2016). In the biomass burning-dominated regions (i.e.,
816 SEA, CF and AMZ), AOD had a significant negative correlation with
817 humidity-related meteorological parameters (such as surface precipitation, RH, and
818 soil moisture), implying that ambient humidity (including the atmosphere and soil)
819 may be a direct correlation factor in controlling the frequency of biomass-burning
820 events (Torres et al., 2010). In contrast, in the regions dominated by anthropogenic
821 aerosols, the correlation was regionally dependent, and their signs differed from place
822 to place.

823 Correlation analysis cannot directly identify the main factors affecting the
824 inter-decadal change of AOD in different regions. Here, MLR models were used to
825 diagnose the influences of local anthropogenic emissions and other meteorological
826 parameters on the inter-decadal variation of AOD over the 12 ROIs. Figure 12 shows
827 the time series of monthly mean MERRA-2 and MLR model-predicted normalized

828 AOD anomalies, which used the emission factors, meteorological parameters, and
829 both, as input predictors, respectively, over the 12 ROIs for the whole study period
830 (1980–2014). Similar comparisons for the two individual periods (i.e., 1980–1997 and
831 1998–2014) are also presented in Figs. S19 and 20, respectively. Table S2 summarizes
832 the predictors included in the MLR models and their performance for the three
833 different periods over each ROI. The MLR models with both emissions and
834 meteorological parameters as predictors generally reproduced the AOD values in most
835 regions during 1980–2014, except for high AOD values (Fig.12), which is discussed
836 below. For all the ROIs, the MLR models explained most of the MERRA-2 AOD
837 variability ($R^2 = 0.42\text{--}0.76$). However, when meteorology and emissions alone were
838 used as predictors, there were considerable differences in different ROIs. When
839 emission factors alone were used as the predictor, it could account for more than 35%
840 of the AOD variability in regions dominated by anthropogenic aerosols and biomass
841 burning [except NEA (14%)], with the largest explanation occurring in NC (58%). In
842 contrast, in the mineral dust–dominated regions (the SD and ME), emission factors
843 contributed little ($< 0.05\%$) to the inter-annual variation in AOD (Figs. 11g and i).
844 Moreover, emission factors contributed 37% of the AOD variability in NWC, which is
845 mainly because of the strong anthropogenic emission sources in northern Xinjiang
846 (mainly encompassing Urumqi, Korla, Kashgar, etc.). However, compared with
847 meteorological factors, emissions were not the main factors driving the inter-annual
848 change of AOD (Fig. 12e).

849 On the other hand, when meteorological factors were used as predictors in the
850 MLR models, it was surprising that they explained a larger proportion of the AOD
851 changes in all ROIs, except NC and SEA, where emission factors accounted for
852 slightly lower AOD changes of 42% and 33%, respectively. Further analysis indicated
853 that this difference in contribution between emissions and meteorology seemed to be
854 greater for the two shorter periods of 1980–1997 and 1998–2017 (see Figs. S19 and
855 20). Besides, it should also be noted that the total explained variances of the MLR
856 model for 1980–1997 were generally lower than those of the MLR model for 1998–
857 2014, in all ROIs. The difference can be explained by two reasons: (1) a greater
858 number of high AOD anomaly values occurred during the period 1980–1997 (Figs. 12
859 and S19), especially in relation to the two volcanic eruption events in the 1980s and
860 1990s, which directly reduced the total explained variances of the MLR model,
861 because the model only considers the inter-decadal variations of local emissions and
862 meteorological factors, and the large-scale transport of pollutants is not considered;
863 and (2) meteorology and emissions were confirmed to explain more AOD changes
864 during the period 1998–2014.

865 **3.6 Relative contributions of local emissions and meteorological** 866 **parameters to inter-decadal variations of regional AOD**

867 Application of the LMG method (see Data and Methods section) to the MLR
868 model allowed the relative contributions of each anthropogenic emission type and
869 meteorological factor to the inter-decadal variations or trend of regional AOD to be

870 quantified. Figure 13 shows the relative contributions of the local emissions and
871 meteorological factors to the changes in regional AOD for the period 1980–2014, as
872 well as for 1980–1997 and 1998–2014, using both emissions and meteorology as
873 predictors in the MLR model. During the period 1980–2014, over the anthropogenic
874 aerosol–dominant regions, SO₂ was the dominant emissions driving factor, explaining
875 24.9%, 15.2%, 32.6%, 21.7% and 12.7% of the variance of AOD over NC, SC, SA,
876 WEU and the EUS, respectively (also see Table S3). The above results also confirm
877 that particulate sulfate is the main contributor to fine-mode AOD in anthropogenic
878 aerosol–dominant regions (Itahashi et al., 2012; David et al., 2018). Meanwhile, wind
879 speed (including surface and upper wind speed) was the dominant meteorological
880 driving factor, explaining 11.4%, 14.2 % and 17.9% of the variance of AOD over NC,
881 SC and the EUS, respectively. In addition, planetary boundary layer height,
882 temperature (including surface temperature, upper temperature, and the temperature
883 difference between the surface and upper atmosphere) and RH (including surface and
884 upper RH) were the strongest meteorological driving factors over NEA, SA and WEU,
885 contributing 30.2%, 15.9% and 21.5%, respectively.

886 On the contrary, over the biomass burning–dominant regions, BC (OC) was the
887 dominant emissions driving factor over SEA (AMZ), explaining 27.7% (24.0%) of the
888 variance of AOD. Meanwhile, soil moisture and RH were the top meteorological
889 driving factors over SEA and AMZ, and CF, contributing 11.7% and 35.5%, and
890 28.5%, respectively. Furthermore, over the dust-dominant regions, wind speed was
891 the strongest meteorological driving factor, explaining 30.3% and 29.8% of the
892 variance in AOD over NWC and the SD, respectively. Different from wind speed
893 being the primary meteorological driving factor over NWC and the SD, it was the
894 second most important factor over the ME, while sea level pressure was the primary
895 driving factor, accounting for 60.9% of the variation in AOD. This large variance
896 explained by sea level pressure and significant anti-correlations of the AOD with it
897 (see Fig. S18c), further confirms the previous studies’ findings that frequent
898 sandstorms over the ME often correspond to large horizontal pressure gradient
899 differences caused by the enhanced high-pressure system across the eastern
900 Mediterranean Sea and enhanced low-pressure system across Iran and Afghanistan
901 (Hamidi et al., 2013; Yu et al., 2016).

902 By comparing the estimated results of the two independent study periods (i.e.,
903 1980–1997 and 1998–2014), it was found that in almost all ROIs (except NC and
904 AMZ), meteorological factors contributed a larger explained proportion of AOD
905 changes during 1998–2014, which indicates that meteorological factors seem to be
906 becoming increasingly more important in dominating the inter-decadal change of
907 regional AOD. It is worth noting that, in addition to the increased explained
908 proportion of SO₂ and BC, among these meteorological factors, the role of
909 diffusion-related parameters (such as horizontal and vertical wind speed, representing
910 horizontal and vertical diffusion, respectively) seems to be the most prominent. This
911 is consistent with the findings of Gui et al. (2019), who found wind speed to be the
912 dominant meteorological driver for decadal changes in fine particulate matter over SC,

913 based upon a 19-yr record of satellite-retrieved fine particulate matter data (1998–
914 2016).

915 **4 Conclusions and implications**

916 This paper presents a comprehensive assessment of the global and regional AOD
917 trends over the past 37 years (1980–2016), based on the reanalysis MERRA-2 AOD
918 dataset. AOD observations from both AERONET and CARSNET stations were used
919 to assess the performance of the MERRA-2 AOD dataset on global and regional
920 scales prior to calculating the global and regional AOD trends. Satellite retrievals
921 from MODIS/Terra and MISR were then used to estimate the AOD annual and
922 seasonal trends and compare them with the MERRA-2 results. Finally, the stepwise
923 MLR and LMG methods were jointly applied to quantify the influences of emission
924 factors and meteorological parameters on the inter-decadal changes in AOD over 12
925 ROIs during the three periods of 1980–2014, 1980–1997 and 1998–2014.

926 Results showed that the MERRA-2 AOD was comparable in accuracy with the
927 satellite-retrieved AOD, albeit there was slight overestimation in the United States,
928 southern South America and Australia and underestimation in the NC, SA, CF and
929 SEA when compared with the ground-based AERONET and CARSNET AOD.
930 MERRA-2 was proven to be capable of estimating the long-term variability and trend
931 of AOD, owing to its good accuracy and continuous and complete spatiotemporal
932 resolution. It was revealed that, in general, MERRA-2 was able to quantitatively
933 reproduce the AOD annual and seasonal trends (especially decadal trends) during the
934 overlapping years (2001–2016), as observed by the MODIS/Terra, albeit some
935 discrepancies (caused by the insufficient sample size) were found when compared to
936 MISR. The resulting trend analyses based upon the MERRA-2 data from 1980 to
937 2016 showed that the global annual trend of AOD during this period, although
938 significantly ($p < 0.05$) weakly negative (i.e., -0.00068 yr^{-1}), was essentially
939 negligible when compared to the magnitudes of regional AOD trends. On regional
940 scales, sliding trend analyses suggested that the inter-decadal trends of AOD in
941 different periods could be significantly different. It was noted that, during the entire
942 study period (1980–2016), the EUS and WEU showed a non-monotonous decreasing
943 trend accompanied by occasional fluctuations in the 1980s and 1990s, responding to
944 the decrease in pollutant emissions, but the intensity of this downward tendency has
945 slowed over the recent decade. In contrast, AODs in NC and SC experienced a
946 sustained and significant upward trend before ~2006, and then the trend shifted from
947 upward to downward due to the Chinese government's emissions-reduction policy. In
948 addition to the negligible downward trend in the 1980s and 1990s, SA showed overall
949 significant positive trends throughout the study period. Moreover, the two large
950 volcanic eruptions that occurred in the 1980s and 1990s not only greatly affected the
951 short-term changes in local aerosol loading, but also impacted significantly on the
952 inter-annual trend of the regional AOD around the world. This highlights the
953 importance of examining the effects of trans-regional pollutant transport on decadal or
954 temporal shifts in local AOD trends.

955 To diagnose the influences of local anthropogenic emissions and other

956 meteorological parameters on the inter-decadal variation of regional AODs, statistical
957 MLR models that estimated AOD monthly values over each ROI as a function of local
958 emissions factors and various meteorological variables were developed. The modeled
959 AODs using emission factors, meteorological parameters, and both, as input
960 predictors in the MLR models were compared during three individual periods (i.e.,
961 1980–2014, 1980–1997 and 1998–2014). In general, the MLR models with both
962 emissions and meteorological parameters as predictors could account for 42%–76% of
963 the variability of the MERRA-2 AOD, depending on the ROI. However, when
964 meteorology and emissions alone were used as predictors, there were considerable
965 differences in different ROIs. During 1980–2014, compared with the emission factors
966 (0%–56%), it was found that meteorological parameters explained a larger proportion
967 of the AOD changes (20.4%–72.8%) over all ROIs (except NC and SEA). Besides,
968 further analysis also showed that this dominant driving role of meteorological
969 parameters was stronger during the other two periods.

970 The LMG method for MLR models suggested that SO₂ was the dominant
971 emissions driving factor, explaining 24.9%, 15.2%, 32.6%, 21.7% and 12.7% of the
972 variance of AOD over NC, SC, SA, WEU and the EUS, respectively. In contrast, BC
973 (OC) was the dominant emissions driving factor over SEA (AMZ), explaining 27.7%
974 (24.0%) of the variance of AOD. For meteorological driving factors, over the mineral
975 dust–dominant regions, wind speed was the top driving factor, explaining 30.3% and
976 29.8% of the variance of AOD over NWC and the SD. Meanwhile, soil moisture and
977 RH were the strongest meteorological driving factors over SEA and AMZ, and CF,
978 contributing 11.7% and 35.5%, and 28.5%, respectively. Notably, the performance of
979 the MLR model in 1980–1997 was significantly worse than that in 1998–2014, which
980 can mainly be attributed to the fact that the statistical model used in this study did not
981 take into account the impact of trans-regional transport. Consequently, the model
982 failed to capture the abnormally high values of regional AOD caused by trans-regional
983 transport during 1980–1997. Finally, deeper insight into the influence of emissions
984 and meteorological factors, as well as the influence of atmospheric transport, on the
985 inter-decadal change in regional AOD, will be provided in future modeling studies.

986

987 **Data availability:**

988 The CARSNET AOD dataset used in the study can be requested by contacting the
989 corresponding author.

990

991 **Competing interests:**

992 The authors declare that they have no conflict of interest.

993

994 **Author contribution:**

995 All authors contributed to shaping up the ideas and reviewing the paper. HC, KG and
996 XZ designed and implemented the research, as well as prepared the manuscript; HC,

997 KG and YW contributed to analysis of the MERRA-2, MODIS and MISR dataset; HC,
998 XX, BNH, PG, and EGA contributed to the CARSNET data retrieval; HC, KG, YW,
999 HW, YZ, and HZ carried out the CARSNET observations; XX, BNH, PG, and EGA
1000 provided constructive comments on this research
1001

1002 **Acknowledgements:**

1003 This work was supported by grants from the National Science Fund for Distinguished
1004 Young Scholars (41825011), the National Key R & D Program Pilot Projects of China
1005 (2016YFA0601901 and 2016YFC0203304), National Natural Science Foundation of
1006 China (41590874), the CAMS Basis Research Project (2017Z011), the European
1007 Union Seventh Framework Programme (FP7/2007-2013) under grant agreement no.
1008 262254, and the AERONET-Europe ACTRIS-2 program, European Union's Horizon
1009 2020 research and innovation programme under grant agreement no. 654109. NASA's
1010 global modeling and assimilation office is gratefully acknowledged for making the
1011 MERRA-2 aerosol reanalysis publicly accessible
1012 (<https://disc.gsfc.nasa.gov/daac-bin/FTPSubset2.pl>). Thanks are also extended to the
1013 PKU emissions inventory research group (<http://inventory.pku.edu.cn/home.html>) and
1014 AERONET networks (<https://aeronet.gsfc.nasa.gov/>) for making their data available
1015 online, as well as the GES-DISC for providing gridded AOD products of MODIS and
1016 MISR through their Giovanni website (<https://giovanni.gsfc.nasa.gov/giovanni/>). All
1017 figures in this study were produced by the open source software of MeteoInfoLab
1018 from Meteoinfo (Wang, 2019), <http://www.meteothink.org/index.html>.

1019 **References**

- 1020 Ackerman, A. S., Toon, O. B., Stevens, D. E., Heymsfield, A. J., Ramanathan, V. and
1021 Welton, E. J.: Reduction of tropical cloudiness by soot, *Science*, 288(5468),
1022 1042-1047, doi:10.1126/science.288.5468.1042, 2000.
- 1023 Altland, H. W., Freund, R. J. and Wilson, W. J.: Regression Analysis: Statistical
1024 Modeling of a Response Variable, *Technometrics*, doi:10.2307/1271353, 2006.
- 1025 An, L., Che, H., Xue, M., Zhang, T., Wang, H., Wang, Y., Zhou, C., Zhao, H., Gui,
1026 K., Zheng, Y., Sun, T., Liang, Y., Sun, E., Zhang, H. and Zhang, X.: Temporal and
1027 spatial variations in sand and dust storm events in East Asia from 2007 to 2016:
1028 Relationships with surface conditions and climate change, *Sci. Total Environ.*, 633,
1029 doi:10.1016/j.scitotenv.2018.03.068, 2018.
- 1030 Andreae, M. O.: Correlation between cloud condensation nuclei concentration and
1031 aerosol optical thickness in remote and polluted regions, *Atmos. Chem. Phys.*,
1032 doi:10.5194/acp-9-543-2009, 2009.
- 1033 Barnett, V., Neter, J. and Wasserman, W.: *Applied Linear Statistical Models.*, J. R.
1034 Stat. Soc. Ser. A, doi:10.2307/2984653, 2006.
- 1035 Bi, J.: A review of statistical methods for determination of relative importance of
1036 correlated predictors and identification of drivers of consumer liking, *J. Sens. Stud.*,
1037 27(2), 87–101, doi:10.1111/j.1745-459X.2012.00370.x, 2012.
- 1038 Bluth, G. J. S., Doiron, S. D., Schnetzler, C. C., Krueger, A. J. and Walter, L. S.:

1039 Global tracking of the SO₂ clouds from the June, 1991 Mount Pinatubo eruptions,
1040 *Geophys. Res. Lett.*, doi:10.1029/91GL02792, 1992.

1041 Buchard, V., Randles, C. A., da Silva, A. M., Darmenov, A., Colarco, P. R.,
1042 Govindaraju, R., Ferrare, R., Hair, J., Beyersdorf, A. J., Ziemba, L. D. and Yu, H.:
1043 The MERRA-2 aerosol reanalysis, 1980 onward. Part II: Evaluation and case
1044 studies, *J. Clim.*, 30(17), 6851–6872, doi:10.1175/JCLI-D-16-0613.1, 2017.

1045 Che, H., Zhang, X., Li, Y., Zhou, Z. and Qu, J. J.: Horizontal visibility trends in China
1046 1981-2005, *Geophys. Res. Lett.*, 34(24), 1–5, doi:10.1029/2007GL031450, 2007.

1047 Che, H., Zhang, X., Chen, H., Damiri, B., Goloub, P., Li, Z., Zhang, X., Wei, Y.,
1048 Zhou, H., Dong, F., Li, D. and Zhou, T.: Instrument calibration and aerosol optical
1049 depth validation of the China aerosol remote sensing network, *J. Geophys. Res.*
1050 *Atmos.*, doi:10.1029/2008JD011030, 2009.

1051 Che, H., Xia, X., Zhu, J., Li, Z., Dubovik, O., Holben, B., Goloub, P., Chen, H.,
1052 Estelles, V., Cuevas-Agulló E., Blarel, L., Wang, H., Zhao, H., Zhang, X., Wang,
1053 Y., Sun, J., Tao, R., Zhang, X. and Shi, G.: Column aerosol optical properties and
1054 aerosol radiative forcing during a serious haze-fog month over North China Plain
1055 in 2013 based on ground-based sunphotometer measurements, *Atmos. Chem. Phys.*,
1056 14(4), 2125–2138, doi:10.5194/acp-14-2125-2014, 2014.

1057 Che, H., Zhang, X. Y., Xia, X., Goloub, P., Holben, B., Zhao, H., Wang, Y., Zhang, X.
1058 C., Wang, H., Blarel, L., Damiri, B., Zhang, R., Deng, X., Ma, Y., Wang, T., Geng,
1059 F., Qi, B., Zhu, J., Yu, J., Chen, Q. and Shi, G.: Ground-based aerosol climatology
1060 of China: Aerosol optical depths from the China Aerosol Remote Sensing Network
1061 (CARSNET) 2002-2013, *Atmos. Chem. Phys.*, 15(13), 7619–7652,
1062 doi:10.5194/acp-15-7619-2015, 2015.

1063 Che, H., Qi, B., Zhao, H., Xia, X., Eck, T. F., Goloub, P., Dubovik, O., Estelles, V.,
1064 Cuevas-Agulló E., Blarel, L., Wu, Y., Zhu, J., Du, R., Wang, Y., Wang, H., Gui,
1065 K., Yu, J., Zheng, Y., Sun, T., Chen, Q., Shi, G. and Zhang, X.: Aerosol optical
1066 properties and direct radiative forcing based on measurements from the China
1067 Aerosol Remote Sensing Network (CARSNET) in eastern China, *Atmos. Chem.*
1068 *Phys.*, 18(1), 405–425, doi:10.5194/acp-18-405-2018, 2018.

1069 Chen, J., Li, C., Ristovski, Z., Milic, A., Gu, Y., Islam, M. S., Wang, S., Hao, J.,
1070 Zhang, H., He, C., Guo, H., Fu, H., Miljevic, B., Morawska, L., Thai, P., LAM, Y.
1071 F., Pereira, G., Ding, A., Huang, X. and Dumka, U. C.: A review of biomass
1072 burning: Emissions and impacts on air quality, health and climate in China, *Sci.*
1073 *Total Environ.*, doi:10.1016/j.scitotenv.2016.11.025, 2017.

1074 Chin, M., Ginoux, P., Kinne, S., Torres, O., Holben, B. N., Duncan, B. N., Martin, R.
1075 V., Logan, J. A., Higurashi, A. and Nakajima, T.: Tropospheric Aerosol Optical
1076 Thickness from the GOCART Model and Comparisons with Satellite and Sun
1077 Photometer Measurements, *J. Atmos. Sci.*, 59(3), 461–483,
1078 doi:10.1175/1520-0469(2002)059<0461:TAOTFT>2.0.CO;2, 2002.

1079 Chin, M., Diehl, T., Tan, Q., Prospero, J. M., Kahn, R. A., Remer, L. A., Yu, H.,
1080 Sayer, A. M., Bian, H., Geogdzhayev, I. V., Holben, B. N., Howell, S. G., Huebert,
1081 B. J., Hsu, N. C., Kim, D., Kucsera, T. L., Levy, R. C., Mishchenko, M. I., Pan, X.,
1082 Quinn, P. K., Schuster, G. L., Streets, D. G., Strode, S. A. and Torres, O.:

1083 Multi-decadal aerosol variations from 1980 to 2009: A perspective from
1084 observations and a global model, *Atmos. Chem. Phys.*, 14(7), 3657–3690,
1085 doi:10.5194/acp-14-3657-2014, 2014.

1086 Cohen, A. J., Brauer, M., Burnett, R., Anderson, H. R., Frostad, J., Estep, K.,
1087 Balakrishnan, K., Brunekreef, B., Dandona, L., Dandona, R., Feigin, V., Freedman,
1088 G., Hubbell, B., Jobling, A., Kan, H., Knibbs, L., Liu, Y., Martin, R., Morawska, L.,
1089 Pope, C. A., Shin, H., Straif, K., Shaddick, G., Thomas, M., van Dingenen, R., van
1090 Donkelaar, A., Vos, T., Murray, C. J. L. and Forouzanfar, M. H.: Estimates and
1091 25-year trends of the global burden of disease attributable to ambient air pollution:
1092 an analysis of data from the Global Burden of Diseases Study 2015, *Lancet*,
1093 389(10082), 1907–1918, doi:10.1016/S0140-6736(17)30505-6, 2017.

1094 Colarco, P., Da Silva, A., Chin, M. and Diehl, T.: Online simulations of global aerosol
1095 distributions in the NASA GEOS-4 model and comparisons to satellite and
1096 ground-based aerosol optical depth, *J. Geophys. Res. Atmos.*, 115(14),
1097 doi:10.1029/2009JD012820, 2010.

1098 David, L. M., Ravishankara, A. R., Kodros, J. K., Venkataraman, C., Sadavarte, P.,
1099 Pierce, J. R., Chaliyakunnel, S. and Millet, D. B.: Aerosol Optical Depth Over
1100 India, *J. Geophys. Res. Atmos.*, doi:10.1002/2017JD027719, 2018.

1101 Diner, D. J., Beckert, J. C., Reilly, T. H., Bruegge, C. J., Conel, J. E., Kahn, R. A.,
1102 Martonchik, J. V., Ackerman, T. P., Davies, R., Gerstel, S. A. W., Gordon, H. R.,
1103 Muller, J. P., Myneni, R. B., Sellers, P. J., Pinty, B. and Verstraete, M. M.:
1104 Multi-angle imaging spectroradiometer (MISR) instrument description and
1105 experiment overview, *IEEE Trans. Geosci. Remote Sens.*, 36(4), 1072–1087,
1106 doi:10.1109/36.700992, 1998.

1107 Eck, T. F., Holben, B. N., Reid, J. S., Dubovik, O., Smirnov, A., O’Neill, N. T.,
1108 Slutsker, I. and Kinne, S.: Wavelength dependence of the optical depth of biomass
1109 burning, urban, and desert dust aerosols, *J. Geophys. Res.*,
1110 doi:10.1029/1999JD900923, 1999.

1111 Edgar: EDGAR - Emission Database for Global Atmospheric Research, *Glob. Emiss.*
1112 EDGAR v4.2 (November 2011), doi:10.2904/EDGARv4.2, 2011.

1113 Fan, A., Chen, W., Liang, L., Sun, W., Lin, Y., Che, H. and Zhao, X.: Evaluation and
1114 comparison of long-term MODIS C5.1 and C6 products against AERONET
1115 observations over China, *Remote Sens.*, 9(12), 1–16, doi:10.3390/rs9121269, 2017.

1116 Feng, Y., Chen, D., Ouyang, X. and Zhang, X.: Variability of satellite-based total
1117 aerosols and the relationship with emission, meteorology and landscape in North
1118 China during 2000–2016, *Environ. Earth Sci.*, 77(13), 1–11,
1119 doi:10.1007/s12665-018-7685-y, 2018.

1120 Field, A.: *Discovering Statistics Using SPSS.*, 2005.

1121 Gao, M., Ji, D., Liang, F. and Liu, Y.: Attribution of aerosol direct radiative forcing in
1122 China and India to emitting sectors, *Atmos. Environ.*, 190, 35–42,
1123 doi:10.1016/j.atmosenv.2018.07.011, 2018.

1124 Gelaro, R., McCarty, W., Suárez, M. J., Todling, R., Molod, A., Takacs, L., Randles,
1125 C. A., Darmenov, A., Bosilovich, M. G., Reichle, R., Wargan, K., Coy, L.,
1126 Cullather, R., Draper, C., Akella, S., Buchard, V., Conaty, A., da Silva, A. M., Gu,

1127 W., Kim, G. K., Koster, R., Lucchesi, R., Merkova, D., Nielsen, J. E., Partyka, G.,
1128 Pawson, S., Putman, W., Rienecker, M., Schubert, S. D., Sienkiewicz, M. and Zhao,
1129 B.: The modern-era retrospective analysis for research and applications, version 2
1130 (MERRA-2), *J. Clim.*, 30(14), 5419–5454, doi:10.1175/JCLI-D-16-0758.1, 2017.

1131 Goldammer, J. G.: History of equatorial vegetation fires and fire research in Southeast
1132 Asia before the 1997-98 episode: A reconstruction of creeping environmental
1133 changes, *Mitig. Adapt. Strateg. Glob. Chang.*, doi:10.1007/s11027-006-9044-7,
1134 2007.

1135 Grömping, U.: Relative importance for linear regression in R: the package relaimpo, *J.*
1136 *Stat. Softw.*, doi:10.1016/j.foreco.2006.08.245, 2006.

1137 Gui, K., Che, H., Chen, Q., An, L., Zeng, Z., Guo, Z., Zheng, Y., Wang, H., Wang, Y.,
1138 Yu, J. and Zhang, X.: Aerosol optical properties based on ground and satellite
1139 retrievals during a serious haze episode in December 2015 over Beijing,
1140 *Atmosphere (Basel)*, 7(5), doi:10.3390/atmos7050070, 2016.

1141 Gui, K., Che, H., Wang, Y., Wang, H., Zhang, L., Zhao, H., Zheng, Y., Sun, T. and
1142 Zhang, X.: Satellite-derived PM_{2.5} concentration trends over Eastern China from
1143 1998 to 2016 : Relationships to emissions and meteorological, *Environ. Pollut.*, 247,
1144 1125–1133, doi:10.1016/j.envpol.2019.01.056, 2019.

1145 Hair, J. F., Black, W. C., Babin, B. J. and Anderson, R. E.: *Multivariate Data Analysis*
1146 (7th Edition)., 2010.

1147 Hamidi, M., Kavianpour, M. R. and Shao, Y.: Synoptic analysis of dust storms in the
1148 Middle East, *Asia-Pacific J. Atmos. Sci.*, 49(3), 279–286,
1149 doi:10.1007/s13143-013-0027-9, 2013.

1150 Hammer, M. S., Martin, R. V., Li, C., Torres, O., Manning, M. and Boys, B. L.:
1151 Insight into global trends in aerosol composition from 2005 to 2015 inferred from
1152 the OMI Ultraviolet Aerosol Index, *Atmos. Chem. Phys.*, 18(11), 8097–8112,
1153 doi:10.5194/acp-18-8097-2018, 2018

1154 Hansen, J., Sato, M. and Ruedy, R.: Radiative forcing and climate response, *J.*
1155 *Geophys. Res. Atmos.*, doi:10.1029/96JD03436, 1997.

1156 He, Q., Zhang, M. and Huang, B.: Spatio-temporal variation and impact factors
1157 analysis of satellite-based aerosol optical depth over China from 2002 to 2015,
1158 *Atmos. Environ.*, 129, 79–90, doi:10.1016/j.atmosenv.2016.01.002, 2016.

1159 Heidinger, A. K., Foster, M. J., Walther, A. and Zhao, X.: The pathfinder
1160 atmospheres-extended avhrr climate dataset, *Bull. Am. Meteorol. Soc.*, 95(6), 909–
1161 922, doi:10.1175/BAMS-D-12-00246.1, 2014.

1162 Hofmann, D. J. and Rosen, J. M.: Stratospheric sulfuric acid fraction and mass
1163 estimate for the 1982 volcanic eruption of El Chichon, *Geophys. Res. Lett.*,
1164 doi:10.1029/GL010i004p00313, 1983.

1165 Holben, B. N., Eck, T. F., Slutsker, I., Tanré D., Buis, J. P., Setzer, A., Vermote, E.,
1166 Reagan, J. A., Kaufman, Y. J., Nakajima, T., Lavenue, F., Jankowiak, I. and
1167 Smirnov, A.: AERONET—A Federated Instrument Network and Data Archive for
1168 Aerosol Characterization, *Remote Sens. Environ.*, 66(1), 1–16,
1169 doi:10.1016/S0034-4257(98)00031-5, 1998.

1170 Hsu, N. C., Gautam, R., Sayer, A. M., Bettenhausen, C., Li, C., Jeong, M. J., Tsay, S.

1171 C. and Holben, B. N.: Global and regional trends of aerosol optical depth over land
1172 and ocean using SeaWiFS measurements from 1997 to 2010, *Atmos. Chem. Phys.*,
1173 12(17), 8037–8053, doi:10.5194/acp-12-8037-2012, 2012.

1174 Huang, Y., Shen, H., Chen, H., Wang, R., Zhang, Y., Su, S., Chen, Y., Lin, N., Zhuo,
1175 S., Zhong, Q., Wang, X., Liu, J., Li, B., Liu, W. and Tao, S.: Quantification of
1176 global primary emissions of PM_{2.5}, PM₁₀, and TSP from combustion and industrial
1177 process sources, *Environ. Sci. Technol.*, doi:10.1021/es503696k, 2014.

1178 Huang, Y., Shen, H., Chen, Y., Zhong, Q., Chen, H., Wang, R., Shen, G., Liu, J., Li,
1179 B. and Tao, S.: Global organic carbon emissions from primary sources from 1960
1180 to 2009, *Atmos. Environ.*, 122, 505–512, doi:10.1016/j.atmosenv.2015.10.017,
1181 2015.

1182 Ikemori, F., Sugata, S., Uranishi, K., Shimadera, H. and Kondo, A.: Impact of field
1183 biomass burning on local pollution and long-range transport of PM_{2.5} in Northeast
1184 Asia, *Environ. Pollut.*, 244, 414–422, doi:10.1016/j.envpol.2018.09.061, 2018.

1185 IPCC: IPCC Fourth Assessment Report: Climate Change 2007., 2007.

1186 Itahashi, S., Uno, I., Yumimoto, K., Irie, H., Osada, K., Ogata, K., Fukushima, H.,
1187 Wang, Z. and Ohara, T.: Interannual variation in the fine-mode MODIS aerosol
1188 optical depth and its relationship to the changes in sulfur dioxide emissions in
1189 China between 2000 and 2010, *Atmos. Chem. Phys.*, 12(5), 2631–2640,
1190 doi:10.5194/acp-12-2631-2012, 2012.

1191 Jiang, J. H., Su, H., Huang, L., Wang, Y., Massie, S., Zhao, B., Omar, A. and Wang,
1192 Z.: Contrasting effects on deep convective clouds by different types of aerosols,
1193 *Nat. Commun.*, 9(1), 3874, doi:10.1038/s41467-018-06280-4, 2018.

1194 Kahn, R. A., Gaitley, B. J., Martonchik, J. V., Diner, D. J., Crean, K. A. and Holben,
1195 B.: Multiangle Imaging Spectroradiometer (MISR) global aerosol optical depth
1196 validation based on 2 years of coincident Aerosol Robotic Network (AERONET)
1197 observations, *J. Geophys. Res. D Atmos.*, 110(10), 1–16,
1198 doi:10.1029/2004JD004706, 2005.

1199 Kahn, R. A., Nelson, D. L., Garay, M. J., Levy, R. C., Bull, M. A., Diner, D. J.,
1200 Martonchik, J. V., Paradise, S. R., Hansen, E. G. and Remer, L. A.: MISR aerosol
1201 product attributes and statistical comparisons with MODIS, *IEEE Trans. Geosci.*
1202 *Remote Sens.*, doi:10.1109/TGRS.2009.2023115, 2009.

1203 Kahn, R. A., Gaitley, B. J., Garay, M. J., Diner, D. J., Eck, T. F., Smirnov, A. and
1204 Holben, B. N.: Multiangle Imaging SpectroRadiometer global aerosol product
1205 assessment by comparison with the Aerosol Robotic Network, *J. Geophys. Res.*
1206 *Atmos.*, 115(23), doi:10.1029/2010JD014601, 2010.

1207 Kim, D., Chin, M., Remer, L. A., Diehl, T., Bian, H., Yu, H., Brown, M. E. and
1208 Stockwell, W. R.: Role of surface wind and vegetation cover in multi-decadal
1209 variations of dust emission in the Sahara and Sahel, *Atmos. Environ.*,
1210 doi:10.1016/j.atmosenv.2016.10.051, 2017.

1211 King, M. D., Menzel, W. P., Kaufman, Y. J., Tanré D., Gao, B. C., Platnick, S.,
1212 Ackerman, S. A., Remer, L. A., Pincus, R. and Hubanks, P. A.: Cloud and aerosol
1213 properties, precipitable water, and profiles of temperature and water vapor from
1214 MODIS, *IEEE Trans. Geosci. Remote Sens.*, 41, 442–456,

1215 doi:10.1109/TGRS.2002.808226, 2003.

1216 Kirchner, I., Stenchikov, G. L., Graf, H. F., Robock, A. and Antuña, J. C.: Climate
1217 model simulation of winter warming and summer cooling following the 1991
1218 Mount Pinatubo volcanic eruption, *J. Geophys. Res. Atmos.*,
1219 doi:10.1029/1999JD900213, 1999.

1220 Klingmüller, K., Pozzer, A., Metzger, S., Stenchikov, G. L. and Lelieveld, J.: Aerosol
1221 optical depth trend over the Middle East, *Atmos. Chem. Phys.*, 16(8), 5063–5073,
1222 doi:10.5194/acp-16-5063-2016, 2016.

1223 De Leeuw, G., Sogacheva, L., Rodriguez, E., Kourtidis, K., Georgoulas, A. K.,
1224 Alexandri, G., Amiridis, V., Proestakis, E., Marinou, E., Xue, Y. and Van Der A,
1225 R.: Two decades of satellite observations of AOD over mainland China using
1226 ATSR-2, AATSR and MODIS/Terra: Data set evaluation and large-scale patterns,
1227 *Atmos. Chem. Phys.*, 18(3), 1573–1592, doi:10.5194/acp-18-1573-2018, 2018.

1228 Lelieveld, J., Evans, J. S., Fnais, M., Giannadaki, D. and Pozzer, A.: The contribution
1229 of outdoor air pollution sources to premature mortality on a global scale, *Nature*,
1230 525(7569), 367–371, doi:10.1038/nature15371, 2015.

1231 Lee, H., Kalashnikova, O. V., Suzuki, K., Braverman, A., Garay, M. J. and Kahn, R.
1232 A.: Climatology of the aerosol optical depth by components from the Multi-angle
1233 Imaging SpectroRadiometer (MISR) and chemistry transport models, *Atmos.*
1234 *Chem. Phys.*, 16(10), 6627–6640, doi:10.5194/acp-16-6627-2016, 2016.

1235 Levy, R. C., Remer, L. A., Kleidman, R. G., Mattoo, S., Ichoku, C., Kahn, R. and Eck,
1236 T. F.: Global evaluation of the Collection 5 MODIS dark-target aerosol products
1237 over land, *Atmos. Chem. Phys.*, 10(21), 10399–10420,
1238 doi:10.5194/acp-10-10399-2010, 2010.

1239 Levy, R. C., Mattoo, S., Munchak, L. A., Remer, L. A., Sayer, A. M., Patadia, F. and
1240 Hsu, N. C.: The Collection 6 MODIS aerosol products over land and ocean, *Atmos.*
1241 *Meas. Tech.*, 6(11), 2989–3034, doi:10.5194/amt-6-2989-2013, 2013.

1242 Levy, R. C., Munchak, L. A., Mattoo, S., Patadia, F., Remer, L. A. and Holz, R. E.:
1243 Towards a long-term global aerosol optical depth record: Applying a consistent
1244 aerosol retrieval algorithm to MODIS and VIIRS-observed reflectance, *Atmos.*
1245 *Meas. Tech.*, 8(10), 4083–4110, doi:10.5194/amt-8-4083-2015, 2015.

1246 Li, J., Carlson, B. E., Dubovik, O. and Lacis, A. A.: Recent trends in aerosol optical
1247 properties derived from AERONET measurements, *Atmos. Chem. Phys.*, 14(22),
1248 12271–12289, doi:10.5194/acp-14-12271-2014, 2014.

1249 Li, J., Li, C., and Zhao, C.: Different trends in extreme and median surface aerosol
1250 extinction coefficients over China inferred from quality-controlled visibility data,
1251 *Atmos. Chem. Phys.*, 18, 3289–3298, <https://doi.org/10.5194/acp-18-3289-2018>,
1252 2018.

1253 Lindeman, R. H., Merenda, P. F. and Gold, R. Z.: *Introduction to Bivariate and*
1254 *Multivariate Analysis.*, Scott, Foresman, Glenview, Ill., 76(375), 2014.

1255 Liu, J., Rühland, K. M., Chen, J., Xu, Y., Chen, S., Chen, Q., Huang, W., Xu, Q.,
1256 Chen, F. and Smol, J. P.: Aerosol-weakened summer monsoons decrease lake
1257 fertilization on the Chinese Loess Plateau, *Nat. Clim. Chang.*, 7(3), 190–194,
1258 doi:10.1038/nclimate3220, 2017.

1259 Liu, P., Washington, W. M., Meehl, G. A., Wu, G. and Potter, G. L.: Historical and
1260 future trends of the Sahara Desert, *Geophys. Res. Lett.*,
1261 doi:10.1029/2001GL012883, 2001.

1262 Lu, X., Zhang, L., Yue, X., Zhang, J., Jaffe, D. A., Stohl, A., Zhao, Y. and Shao, J.:
1263 Wildfire influences on the variability and trend of summer surface ozone in the
1264 mountainous western United States, *Atmos. Chem. Phys.*,
1265 doi:10.5194/acp-16-14687-2016, 2016.

1266 Ma, Z., Hu, X., Sayer, A. M., Levy, R., Zhang, Q., Xue, Y., Tong, S., Bi, J., Huang, L.
1267 and Liu, Y.: Satellite-based spatiotemporal trends in PM_{2.5} concentrations: China,
1268 2004-2013, *Environ. Health Perspect.*, 124(2), 184–192, doi:10.1289/ehp.1409481,
1269 2016.

1270 Mao, K. B., Ma, Y., Xia, L., Chen, W. Y., Shen, X. Y., He, T. J. and Xu, T. R.:
1271 Global aerosol change in the last decade: An analysis based on MODIS data,
1272 *Atmos. Environ.*, 94, 680–686, doi:10.1016/j.atmosenv.2014.04.053, 2014

1273 McCormick, R. A. and Ludwig, J. H.: Climate modification by atmospheric aerosols,
1274 *Science*, 156(3780), 1358-1359, doi:10.1126/science.156.3780.1358, 1967.

1275 Mehta, M., Singh, R., Singh, A., Singh, N. and Anshumali: Recent global aerosol
1276 optical depth variations and trends - A comparative study using MODIS and MISR
1277 level 3 datasets, *Remote Sens. Environ.*, 181, 137–150,
1278 doi:10.1016/j.rse.2016.04.004, 2016.

1279 Meij, A. De, Pozzer, A. and Lelieveld, J.: Trend analysis in aerosol optical depths and
1280 pollutant emission estimates between 2000 and 2009, *Atmos. Environ.*, 51, 75–85,
1281 doi:10.1016/j.atmosenv.2012.01.059, 2012.

1282 De Meij, A., Pozzer, A. and Lelieveld, J.: Trend analysis in aerosol optical depths and
1283 pollutant emission estimates between 2000 and 2009, *Atmos. Environ.*, 51, 75–85,
1284 doi:10.1016/j.atmosenv.2012.01.059, 2012.

1285 Minguillón, M. C., Brines, M., Pérez, N., Reche, C., Pandolfi, M., Fonseca, A. S.,
1286 Amato, F., Alastuey, A., Lyasota, A., Codina, B., Lee, H. K., Eun, H. R., Ahn, K.
1287 H. and Querol, X.: New particle formation at ground level and in the vertical
1288 column over the Barcelona area, *Atmos. Res.*, doi:10.1016/j.atmosres.2015.05.003,
1289 2015.

1290 Molod, A., Takacs, L., Suarez, M., Bacmeister, J., Song, I.-S. and Eichmann, A.: The
1291 GEOS-5 atmospheric general circulation model: Mean climate and development
1292 from MERRA to Fortuna., 2012.

1293 Molod, A., Takacs, L., Suarez, M. and Bacmeister, J.: Development of the GEOS-5
1294 atmospheric general circulation model: Evolution from MERRA to MERRA2,
1295 *Geosci. Model Dev.*, 8(5), 1339–1356, doi:10.5194/gmd-8-1339-2015, 2015.

1296 Page, S. E., Siegert, F., Rieley, J. O., Boehm, H. D. V., Jaya, A. and Limin, S.: The
1297 amount of carbon released from peat and forest fires in Indonesia during 1997,
1298 *Nature*, doi:10.1038/nature01131, 2002.

1299 Pozzer, A., De Meij, A., Yoon, J., Tost, H., Georgoulias, A. K. and Astitha, M.: AOD
1300 trends during 2001-2010 from observations and model simulations, *Atmos. Chem.*
1301 *Phys.*, 15(10), 5521–5535, doi:10.5194/acp-15-5521-2015, 2015.

1302 Proestakis, E., Amiridis, V., Marinou, E., Georgoulias, A. K., Solomos, S., Kazadzis,

1303 S., Chimot, J., Che, H., Alexandri, G., Biniotoglou, I., Daskalopoulou, V.,
1304 Kourtidis, K. A., De Leeuw, G. and Van Der A, R. J.: Nine-year spatial and
1305 temporal evolution of desert dust aerosols over South and East Asia as revealed by
1306 CALIOP, *Atmos. Chem. Phys.*, 18(2), 1337–1362, doi:10.5194/acp-18-1337-2018,
1307 2018.

1308 Qin, W., Liu, Y., Wang, L., Lin, A., Xia, X., Che, H., Bilal, M., Zhang, M., Qin, W.,
1309 Liu, Y., Wang, L., Lin, A., Xia, X., Che, H., Bilal, M. and Zhang, M.:
1310 Characteristic and Driving Factors of Aerosol Optical Depth over Mainland China
1311 during 1980–2017, *Remote Sens.*, 10(7), 1064, doi:10.3390/rs10071064, 2018.

1312 Ramanathan, V., Crutzen, P. J., Kiehl, J. T. and Rosenfeld, D.: Atmosphere: Aerosols,
1313 climate, and the hydrological cycle, *Science*, 294(5549), 2119–2124,
1314 doi:10.1126/science.1064034, 2001.

1315 Remer, L. A., Kaufman, Y. J., Tanré D., Mattoo, S., Chu, D. A., Martins, J. V., Li,
1316 R.-R., Ichoku, C., Levy, R. C., Kleidman, R. G., Eck, T. F., Vermote, E. and
1317 Holben, B. N.: The MODIS Aerosol Algorithm, Products, and Validation, *J. Atmos.*
1318 *Sci.*, 62(4), 947–973, doi:10.1175/JAS3385.1, 2005.

1319 Rosenfeld, D., Zhu, Y., Wang, M., Zheng, Y., Goren, T. and Yu, S.: Aerosol-driven
1320 droplet concentrations dominate coverage and water of oceanic low-level clouds,
1321 *Science*, 363(6427), eaav0566, doi:10.1126/science.aav0566, 2019.

1322 Sarangi, C., Kanawade, V. P., Tripathi, S. N., Thomas, A. and Ganguly, D.:
1323 Aerosol-induced intensification of cooling effect of clouds during Indian summer
1324 monsoon, *Nat. Commun.*, 9(1), doi:10.1038/s41467-018-06015-5, 2018.

1325 Silva, R. A., West, J. J., Zhang, Y., Anenberg, S. C., Lamarque, J. F., Shindell, D. T.,
1326 Collins, W. J., Dalsoren, S., Faluvegi, G., Folberth, G., Horowitz, L. W.,
1327 Nagashima, T., Naik, V., Rumbold, S., Skeie, R., Sudo, K., Takemura, T.,
1328 Bergmann, D., Cameron-Smith, P., Cionni, I., Doherty, R. M., Eyring, V., Josse, B.,
1329 Mackenzie, I. A., Plummer, D., Righi, M., Stevenson, D. S., Strode, S., Szopa, S.
1330 and Zeng, G.: Global premature mortality due to anthropogenic outdoor air
1331 pollution and the contribution of past climate change, *Environ. Res. Lett.*,
1332 doi:10.1088/1748-9326/8/3/034005, 2013.

1333 Smirnov, A., Holben, B. N., Eck, T. F., Dubovik, O. and Slutsker, I.: Cloud-screening
1334 and quality control algorithms for the AERONET database, *Remote Sens. Environ.*,
1335 doi:10.1016/S0034-4257(00)00109-7, 2000.

1336 Song, Z., Fu, D., Zhang, X., Wu, Y., Xia, X. and He, J.: Diurnal and seasonal
1337 variability of PM_{2.5} and AOD in North China plain: Comparison of MERRA-2
1338 products and ground measurements, *Atmos. Environ.*, 191, 70–78,
1339 doi:10.1016/j.atmosenv.2018.08.012, 2018.

1340 Stenchikov, G. L., Kirchner, I., Robock, A., Graf, H. F., Antuña, J. C., Grainger, R. G.,
1341 Lambert, A. and Thomason, L.: Radiative forcing from the 1991 Mount Pinatubo
1342 volcanic eruption, *J. Geophys. Res. Atmos.*, doi:10.1029/98JD00693, 1998.

1343 Su, S., Li, B., Cui, S. and Tao, S.: Sulfur dioxide emissions from combustion in China:
1344 From 1990 to 2007, *Environ. Sci. Technol.*, 45(19), 8403–8410,
1345 doi:10.1021/es201656f, 2011.

1346 Sun, E., Xu, X., Che, H., Tang, Z., Gui, K., An, L., Lu, C. and Shi, G.: Variation in

1347 MERRA-2 aerosol optical depth and absorption aerosol optical depth over China
1348 from 1980 to 2017, *J. Atmos. Solar-Terrestrial Phys.*, 186, 8–19,
1349 doi:10.1016/j.jastp.2019.01.019, 2019.

1350 Sun, T., Che, H., Qi, B., Wang, Y., Dong, Y., Xia, X., Wang, H., Gui, K., Zheng, Y.,
1351 Zhao, H., Ma, Q., Du, R. and Zhang, X.: Aerosol optical characteristics and their
1352 vertical distributions under enhanced haze pollution events: Effect of the regional
1353 transport of different aerosol types over eastern China, *Atmos. Chem. Phys.*, 18(4),
1354 doi:10.5194/acp-18-2949-2018, 2018.

1355 Tai, A. P. K., Mickley, L. J. and Jacob, D. J.: Correlations between fine particulate
1356 matter (PM_{2.5}) and meteorological variables in the United States: Implications for
1357 the sensitivity of PM_{2.5} to climate change, *Atmos. Environ.*,
1358 doi:10.1016/j.atmosenv.2010.06.060, 2010.

1359 Thornhill, G. D., Ryder, C. L., Highwood, E. J., Shaffrey, L. C. and Johnson, B. T.:
1360 The effect of South American biomass burning aerosol emissions on the regional
1361 climate, *Atmos. Chem. Phys.*, doi:10.5194/acp-18-5321-2018, 2018.

1362 Torres, O., Chen, Z., Jethva, H., Ahn, C., Freitas, S. R. and Bhartia, P. K.: OMI and
1363 MODIS observations of the anomalous 2008-2009 Southern Hemisphere biomass
1364 burning seasons, *Atmos. Chem. Phys.*, 10(8), 3505–3513,
1365 doi:10.5194/acp-10-3505-2010, 2010.

1366 Tummon, F., Solmon, F., Liou, C. and Tadross, M.: Simulation of the direct and
1367 semidirect aerosol effects on the southern Africa regional climate during the
1368 biomass burning season, *J. Geophys. Res. Atmos.*, doi:10.1029/2009JD013738,
1369 2010.

1370 Wang, K., Dickinson, R. E. and Liang, S.: Clear sky visibility has decreased over land
1371 globally from 1973 to 2007, *Science*, 323(5920), 1468-1470,
1372 doi:10.1126/science.1167549, 2009.

1373 Wang, R., Tao, S., Shen, H., Huang, Y., Chen, H., Balkanski, Y., Boucher, O., Ciais,
1374 P., Shen, G., Li, W., Zhang, Y., Chen, Y., Lin, N., Su, S., Li, B., Liu, J. and Liu,
1375 W.: Trend in global black carbon emissions from 1960 to 2007, *Environ. Sci.*
1376 *Technol.*, 48(12), 6780–6787, doi:10.1021/es5021422, 2014.

1377 Wang, X., Liu, J., Che, H., Ji, F. and Liu, J.: Spatial and temporal evolution of natural
1378 and anthropogenic dust events over northern China, *Sci. Rep.*, 8(1),
1379 doi:10.1038/s41598-018-20382-5, 2018.

1380 Wang, Y. Q.: An Open Source Software Suite for Multi-Dimensional Meteorological
1381 Data Computation and Visualisation, (1), 1–9, 2019.

1382 Willmott, C. J.: On the validation of models, *Phys. Geogr.*, 2, 184–194,
1383 <https://doi.org/10.1002/joc.2419>, 1981.

1384 Wei, J., Peng, Y., Guo, J. and Sun, L.: Performance of MODIS Collection 6.1 Level 3
1385 aerosol products in spatial- temporal variations over land, *Atmos. Environ.*, 206,
1386 30–44, doi:10.1016/j.atmosenv.2019.03.001, 2019.

1387 Yang, Y., Liao, H. and Lou, S.: Increase in winter haze over eastern China in recent
1388 decades: Roles of variations in meteorological parameters and anthropogenic
1389 emissions, *J. Geophys. Res.*, 121(21), 13,050-13,065, doi:10.1002/2016JD025136,
1390 2016.

1391 Yu, Y., Notaro, M., Kalashnikova, O. V. and Garay, M. J.: Climatology of summer
1392 Shamal wind in the Middle East, *J. Geophys. Res.*, doi:10.1002/2015JD024063,
1393 2016.

1394 Yumimoto, K., Tanaka, T. Y., Oshima, N. and Maki, T.: JRAero: The Japanese
1395 Reanalysis for Aerosol v1.0, *Geosci. Model Dev.*, 10(9), 3225–3253,
1396 doi:10.5194/gmd-10-3225-2017, 2017.

1397 Yue, X., Unger, N., Harper, K., Xia, X., Liao, H., Zhu, T., Xiao, J., Feng, Z. and Li, J.:
1398 Ozone and haze pollution weakens net primary productivity in China, *Atmos.*
1399 *Chem. Phys.*, 17(9), 6073–6089, doi:10.5194/acp-17-6073-2017, 2017.

1400 Zhai, S., Jacob, D. J., Wang, X., Shen, L., Li, K., Zhang, Y., Gui, K., Zhao, T., and
1401 Liao, H.: Fine particulate matter (PM_{2.5}) trends in China, 2013–2018: contributions
1402 from meteorology, *Atmos. Chem. Phys. Discuss.*,
1403 <https://doi.org/10.5194/acp-2019-279>, in review, 2019.

1404 Zhang, H., Shen, Z., Wei, X., Zhang, M. and Li, Z.: Comparison of optical properties
1405 of nitrate and sulfate aerosol and the direct radiative forcing due to nitrate in China,
1406 *Atmos. Res.*, doi:10.1016/j.atmosres.2012.04.020, 2012.

1407 Zhang, J. and Reid, J. S.: A decadal regional and global trend analysis of the aerosol
1408 optical depth using a data-assimilation grade over-water MODIS and Level 2
1409 MISR aerosol products, *Atmos. Chem. Phys.*, 10(22), 10949–10963,
1410 doi:10.5194/acp-10-10949-2010, 2010.

1411 Zhao, B., Jiang, J. H., Gu, Y., Diner, D., Worden, J., Liou, K. N., Su, H., Xing, J.,
1412 Garay, M. and Huang, L.: Decadal-scale trends in regional aerosol particle
1413 properties and their linkage to emission changes, *Environ. Res. Lett.*, 12(5),
1414 doi:10.1088/1748-9326/aa6cb2, 2017.

1415 Zhao, B., Jiang, J. H., Diner, D. J., Su, H., Gu, Y., Liou, K.-N., Jiang, Z., Huang, L.,
1416 Takano, Y., Fan, X. and Omar, A. H.: Intra-annual variations of regional aerosol
1417 optical depth, vertical distribution, and particle types from multiple satellite and
1418 ground-based observational datasets, *Atmos. Chem. Phys.*, 18(15), 11247–11260,
1419 doi:10.5194/acp-18-11247-2018, 2018.

1420 Zheng, B., Tong, D., Li, M., Liu, F., Hong, C., Geng, G., Li, H., Li, X., Peng, L., Qi,
1421 J., Yan, L., Zhang, Y., Zhao, H., Zheng, Y., He, K. and Zhang, Q.: Trends in
1422 China's anthropogenic emissions since 2010 as the consequence of clean air
1423 actions, *Atmos. Chem. Phys.*, doi:10.5194/acp-18-14095-2018, 2018.

1424 Zheng, Y., Che, H., Xia, X., Wang, Y., Wang, H., Wu, Y., Tao, J., Zhao, H., An, L.,
1425 Li, L., Gui, K., Sun, T., Li, X., Sheng, Z., Liu, C., Yang, X., Liang, Y., Zhang, L.,
1426 Liu, C., Kuang, X., Luo, S., You, Y. and Zhang, X.: Five-year observation of
1427 aerosol optical properties and its radiative effects to planetary boundary layer
1428 during air pollution episodes in North China: Intercomparison of a plain site and a
1429 mountainous site in Beijing, *Sci. Total Environ.*,
1430 doi:10.1016/J.SCITOTENV.2019.03.418, 2019.

1431

1432 **Table captions:**

1433 **Table 1.** Prediction variables used in the stepwise MLR models.

1434

1435 **Table 2.** Statistical measures of the three hourly MERRA-2 AOD versus AERONET and
1436 CARSNET AODs over the 12 regions of interest.

1437

1438 **Figure captions:**

1439 **Figure 1.** Geographical locations of the AERONET (yellow dots) and CARSNET sites (magenta
1440 dots) used in this work. The red boxes represent the 12 regions of interest selected in this study:
1441 Northeast Asia (NEA), northern China (NC), southern China (SC), Southeast Asia (SEA),
1442 Northwest China (NWC), South Asia (SA), Middle East (ME), western Europe (WEU), Sahara
1443 Desert (SD), Central Africa (CF), eastern United States (EUS), and Amazon Zone (AMZ).

1444

1445 **Figure 2.** Flowchart with the procedure followed for (a) the evaluation of MERRA-2 global AOD
1446 using the AERONET and CARSNET ground-based reference dataset, and (b) the evaluation of
1447 global and regional AOD trends.

1448

1449 **Figure 3.** Evaluation of the three-hourly MERRA-2 AOD against the (a) AERONET and (b)
1450 CARSNET AODs. The color-coded dots indicate the number of samples. The solid red line is the
1451 line of best fit and the black dashed line is the 1:1 line. For descriptions of statistical metrics, see
1452 the comparison methods section.

1453

1454 **Figure 4.** Comparison of the three-hourly MERRA-2 AOD datasets with AOD observations of
1455 468 AERONET sites worldwide and 37 CARSNET sites in China: site performance maps for the
1456 (a) correlation coefficient (R), (b) mean absolute error (MAE), root-mean-square error (RMSE), (c)
1457 relative mean bias (RMB), (d) mean fractional error (MFE), (e) fractional gross error (FGE), and
1458 (f) the index of agreement (IOA) between MERRA-2 AOD and ground-based AOD observations.
1459 The size of the circles in Fig.4b represents the RMSE and their inner color represents the MAE.
1460 The bars in the lower left inset in each panel represent the frequency distribution histograms for
1461 the R , MAE, RMSE, RMB, MFE, FGE and IOA between MERRA-2 and all ground-based
1462 observations incorporating AERONET and CARSNET, respectively. Note that all sites within
1463 each region of interest (ROI) are integrated to assess the accuracy of the MERRA-2 AOD dataset
1464 in that area. The performance of the MERRA-2 AOD dataset in each ROI is illustrated in Figs. S2
1465 and S3.

1466

1467 **Figure 5.** Temporal evolution of regional monthly averaged AOD for the 12 regions of interest.
1468 Each year is represented by an irregular ring with 12 directions. Each direction of the ring
1469 represents a specific month; the distance from the center of the ring represents the regional
1470 monthly mean AOD value; and the color of the ring represents the year. A special ring colored
1471 cyan represents the monthly mean AOD for the period 1980–2016.

1472

1473 **Figure 6.** Spatial distributions of the linear trends in annual and seasonal MERRA-2 AOD

1474 calculated from the time series value of the de-seasonalized monthly anomaly during (a) 1980–
1475 2016, (b) 1980–1997, and (c) 1998–2016. Only trend values with statistical significance at the 95%
1476 confidence level are shown.

1477

1478 **Figure 7.** Spatial distributions of annual and seasonal trends in AOD calculated from the time
1479 series value of the de-seasonalized monthly anomaly from (a) MERRA-2, (b) MODIS/Terra, and
1480 (c) MISR between 2001 and 2016. Only trend values with statistical significance at the 95%
1481 confidence level are shown.

1482

1483 **Figure 8.** Inter-comparisons of global and regional annual trends in AOD calculated from the time
1484 series value of the de-seasonalized monthly anomaly of MERRA-2, MODIS/Terra and MISR,
1485 during the four periods of 1980–2016, 1980–1997, 1998–2016, and 2001–2016. Error bars
1486 represent the uncertainty associated with the calculated trend. The trend bars with shadow indicate
1487 statistical significance at the 95% confidence level.

1488

1489 **Figure 9.** Sliding-window trend analyses of the annual mean MERRA-2 AOD from 1980 to 2016
1490 over the 12 ROIs (see Fig. 1 for names and locations of regions), with at least 10 years used to
1491 calculate trends. The *x*-axis and *y*-axis indicate the start year and the length of the time series to
1492 calculate the trend, respectively. The colors of rectangles represent the intensity of the trend (units:
1493 /year), and those with black ‘x’ signs indicate linear trends above the 95% significance level.

1494

1495 **Figure 10.** Temporal evolution of sliding decadal trends in the annual and seasonal mean AOD
1496 from MERRA-2, MODIS/Terra and MISR over the 12 ROIs. The trends were calculated for each
1497 10-year interval from 1980 to 2007 for MERRA-2, and from 2001 to 2007 for MODIS/Terra and
1498 MISR. The colors of the rectangles represent the intensity of the decadal trend (units: /year), and
1499 those with black ‘x’ signs indicate linear trends above the 95% significance level.

1500

1501 **Figure 11.** Spatial distributions of linear trends (units: kg/km²/year) in total anthropogenic
1502 emissions of total suspended particles (TSP), SO₂, black carbon (BC), and organic carbon (OC)
1503 during 1980–2014 derived from the Peking University emissions inventory
1504 (<http://inventory.pku.edu.cn/>) (Huang et al., 2014). Only linear trend values with statistical
1505 significance at the 95% confidence level are shown.

1506

1507 **Figure 12.** Time series of MERRA-2 (in black) and modeled AOD monthly normalized anomalies
1508 from 1980 to 2014 over the 12 regions of interest. The coefficient of determination (R^2) of the
1509 regression fit of the stepwise MLR model with emission factors (in blue), meteorology (in green),
1510 and both emissions and meteorology (in red) as predictors are given in the top-right of each panel.

1511

1512 **Figure 13.** The LMG method–estimated relative contributions (%) of total variances in the
1513 stepwise MLR model explained by the local emission factors (left-hand bars) and meteorological
1514 variables (right-hand bars) over the 12 regions of interest during three periods: (a) 1980–1997 (top
1515 panel); (b) 1998–2014 (middle panel); and (c) 1980–2014 (bottom panel). Note that
1516 meteorological parameters were combined as follows: temperature, T (Ts, T₈₅₀, T₇₀₀, T₅₀₀, dT_{900-s},
1517 dT_{850-s}); geopotential height, GH (GH₈₅₀, GH₇₀₀, GH₅₀₀); relative humidity, RH (RH_s, RH₈₅₀, RH₇₀₀,

1518 RH₅₀₀); vertical velocity, Ome (Ome₈₅₀, Ome₇₀₀, Ome₅₀₀); and wind speed, WS (U₈₅₀, U₇₀₀, U₅₀₀,
1519 V₈₅₀, V₇₀₀, V₅₀₀, WS_s, WS₈₅₀, WS₇₀₀, WS₅₀₀, VWS₅₀₀₋₈₅₀). Refer to Table S3 for the detailed
1520 relative contributions of each variable in the stepwise MLR models.

1521 Table 1. Prediction variables used in the stepwise MLR models.

Data type	Variables	Predictors used in the stepwise MLR model ^a	Data source
Emission factors	TSP	Gridded monthly total emissions of total suspended particles	Peking University global emissions inventories at 1° × 1° horizontal resolution (http://inventory.pku.edu.cn/home.html)
	SO ₂	Gridded monthly total emissions of sulfur dioxide	
	BC	Gridded monthly total emissions of black carbon	
	OC	Gridded monthly total emissions of organic carbon	
Meteorological parameters	Pre	Gridded monthly total surface precipitation	MERRA-2 reanalysis dataset at 0.5° × 0.625° horizontal resolution (https://disc.gsfc.nasa.gov/daac-bin/FTPSubset2.pl)
	PBLH	Gridded monthly mean planetary boundary layer height	
	SM	Gridded monthly mean soil moisture at surface	
	SLP	Gridded monthly mean sea level pressure	
	CLF	Gridded monthly mean cloud fraction	
	T _s	Gridded monthly mean surface temperature	
	T	Gridded monthly mean 850-, 700- and 500-hPa temperature	
	dT	Gridded monthly mean temperature difference between 900 hPa and the surface, and 850 hPa and the surface	
	GH	Gridded monthly mean 850-, 700- and 500-hPa geopotential height	
	RH _s	Gridded monthly mean surface relative humidity	
	RH	Gridded monthly mean 850-, 700- and 500-hPa relative humidity	
	Ome	Gridded monthly mean 850-, 700- 500-hPa vertical velocity	
	U	Gridded monthly mean 850-, 700- and 500-hPa zonal wind	
	V	Gridded monthly mean 850-, 700- and 500-hPa meridional wind	
WS _s	Gridded monthly mean surface wind speed		
WS	Gridded monthly mean 850-, 700- and 500-hPa wind speed		
VS ₅₀₀₋₈₅₀ ^b	Gridded monthly mean vertical wind shear between 500 and 850 hPa		

1522 ^aUnits: g/km² (TSP, SO₂, BC, OC); kg/m²/s (Pre); m (PBLH, GH); 1 (SM, CLF); Pa (SLP); K (T, dT); % (RH); pa/s (Ome); and m/s (U, V, WS, VWS₅₀₀₋₈₅₀)

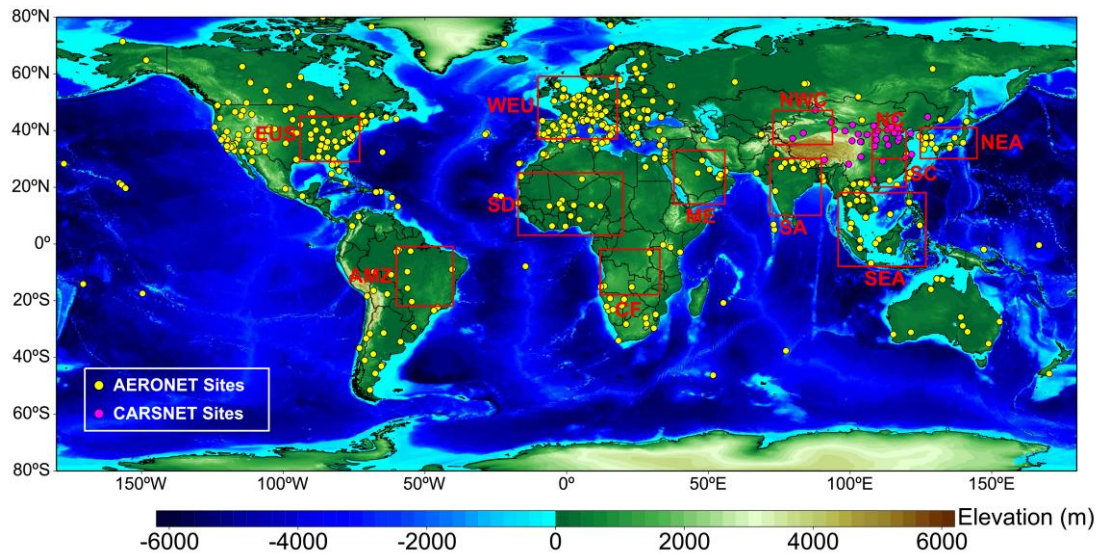
1523 ^bVWS₅₀₀₋₈₅₀ was calculated as $\sqrt{(U_{500} - U_{850})^2 + (V_{500} - V_{850})^2}$

1524

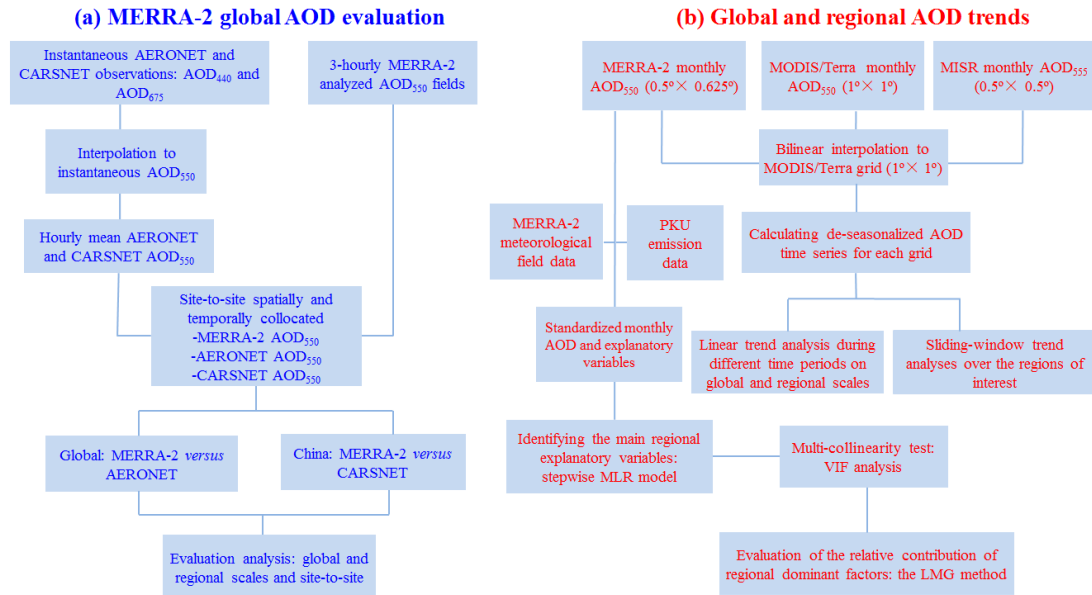
1525 Table 2. Statistical measures of the three hourly MERRA-2 AOD versus AERONET and CARSNET AODs over the 12 regions of interest.

ROIs	Number of sites	Number of collocations	R	MAE	RMSE	RMB	MFE (%)	FGE (%)	IOA
NEA	13	35066	0.79	0.10	0.16	0.93	33.18	-2.65	0.92
NC	3	16782	0.80	0.25	0.42	0.71	45.44	-23.85	0.78
SC	2	3616	0.87	0.08	0.13	1.01	24.73	5.25	0.95
SEA	17	32112	0.79	0.12	0.24	0.84	31.26	-8.52	0.86
NWC	1	4633	0.85	0.03	0.05	1.01	30.74	1.98	0.98
SA	13	33385	0.84	0.11	0.18	0.87	34.54	-8.06	0.93
ME	10	34312	0.95	0.04	0.07	1.02	12.89	4.13	0.98
WEU	81	252767	0.79	0.04	0.07	0.95	32.91	2.01	0.97
SD	14	69982	0.81	0.14	0.20	0.97	33.22	4.40	0.91
CF	5	12380	0.83	0.08	0.14	0.75	35.78	-22.96	0.93
EUS	38	105577	0.70	0.07	0.11	1.11	42.28	17.82	0.94
AMZ	8	21105	0.82	0.08	0.19	0.84	35.84	-1.73	0.89
NC ^a	12	27508	0.70	0.23	0.33	0.71	47.31	-35.45	0.81
SC ^a	2	2346	0.74	0.15	0.21	0.92	30.85	-8.01	0.90
NWC ^a	3	10103	0.67	0.20	0.33	0.69	45.17	-26.00	0.78

1526 ^a indicates the statistical results for CARSNET sites.



1527
 1528 **Figure 1.** Geographical locations of the AERONET (yellow dots) and CARSNET sites (magenta dots) used in this
 1529 work. The red boxes represent the 12 regions of interest selected in this study: Northeast Asia (NEA), northern
 1530 China (NC), southern China (SC), Southeast Asia (SEA), Northwest China (NWC), South Asia (SA), Middle East
 1531 (ME), western Europe (WEU), Sahara Desert (SD), Central Africa (CF), eastern United States (EUS), and Amazon
 1532 Zone (AMZ).
 1533
 1534



1535

1536

Figure 2. Flowchart with the procedure followed for (a) the evaluation of MERRA-2 global AOD using the AERONET and CARSNET ground-based reference dataset, and (b) the evaluation of global and regional AOD trends.

1537

1538

1539

1540

1541

1542

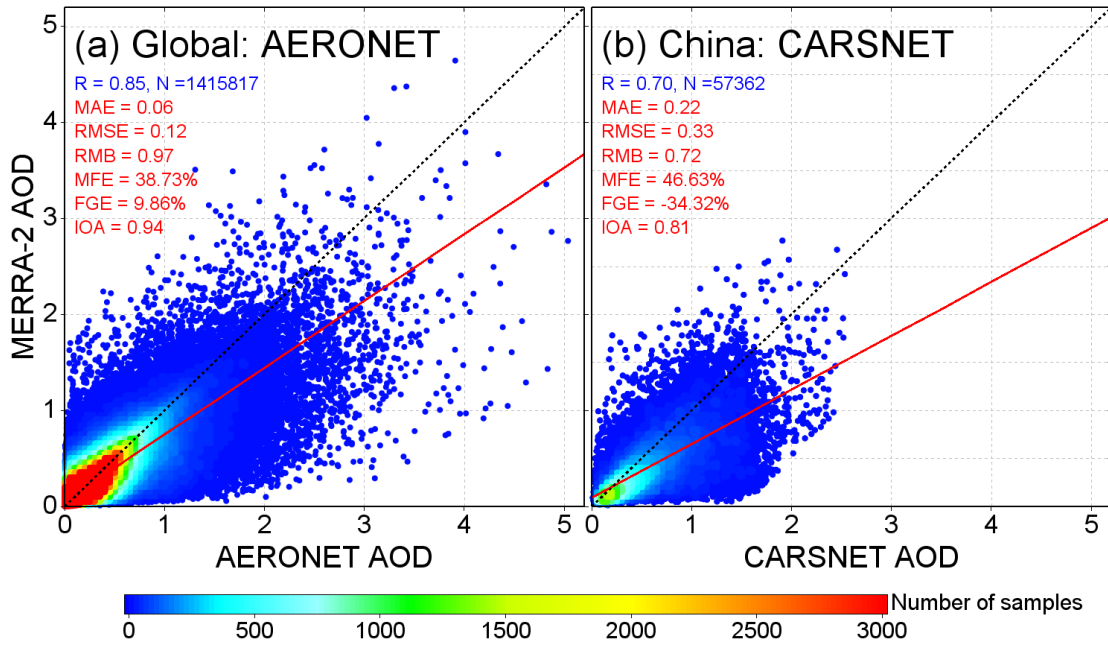
1543

1544

1545

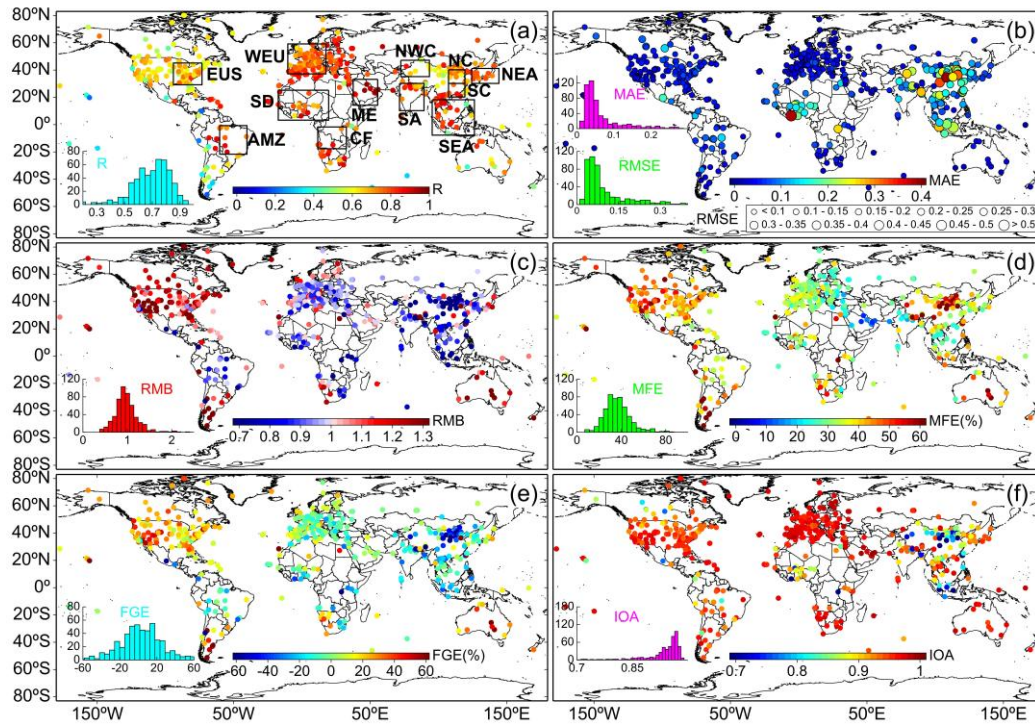
1546

1546



1547
 1548
 1549
 1550
 1551
 1552
 1553
 1554
 1555
 1556
 1557
 1558

Figure 3. Evaluation of the three-hourly MERRA-2 AOD against the (a) AERONET and (b) CARSNET AODs. The color-coded dots indicate the number of samples. The solid red line is the line of best fit and the black dashed line is the 1:1 line. For descriptions of statistical metrics, see the comparison methods section.



1559

1560

Figure 4. Comparison of the three-hourly MERRA-2 AOD datasets with AOD observations of 468 AERONET sites worldwide and 37 CARSNET sites in China: site performance maps for the (a) correlation coefficient (R), (b) mean absolute error (MAE), root-mean-square error (RMSE), (c) relative mean bias (RMB), (d) mean fractional error (MFE), (e) fractional gross error (FGE), and (f) the index of agreement (IOA) between MERRA-2 AOD and ground-based AOD observations. The size of the circles in Fig.4b represents the RMSE and their inner color represents the MAE. The bars in the lower left inset in each panel represent the frequency distribution histograms for the R , MAE, RMSE, RMB, MFE, FGE and IOA between MERRA-2 and all ground-based observations incorporating AERONET and CARSNET, respectively. Note that all sites within each region of interest (ROI) are integrated to assess the accuracy of the MERRA-2 AOD dataset in that area. The performance of the MERRA-2 AOD dataset in each ROI is illustrated in Figs. S2 and S3.

1565

1566

1567

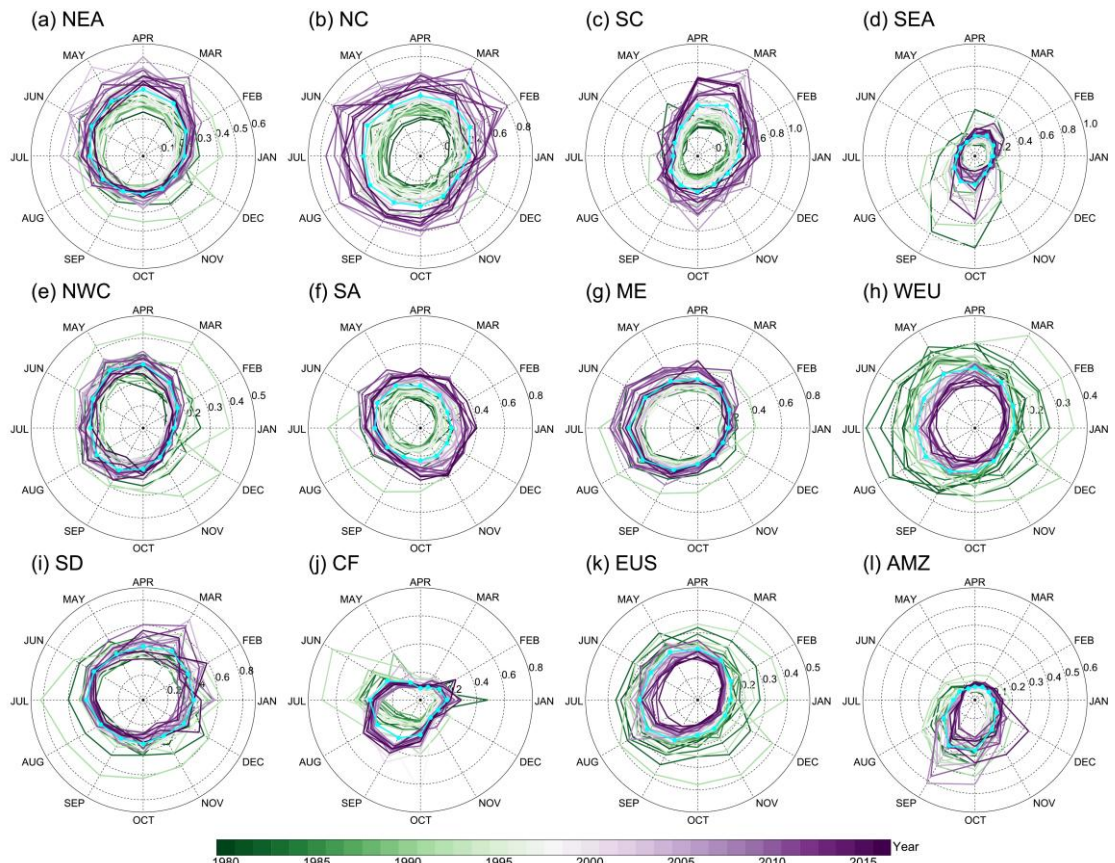
1568

1569

1570

1571

1572



1573

1574

1575

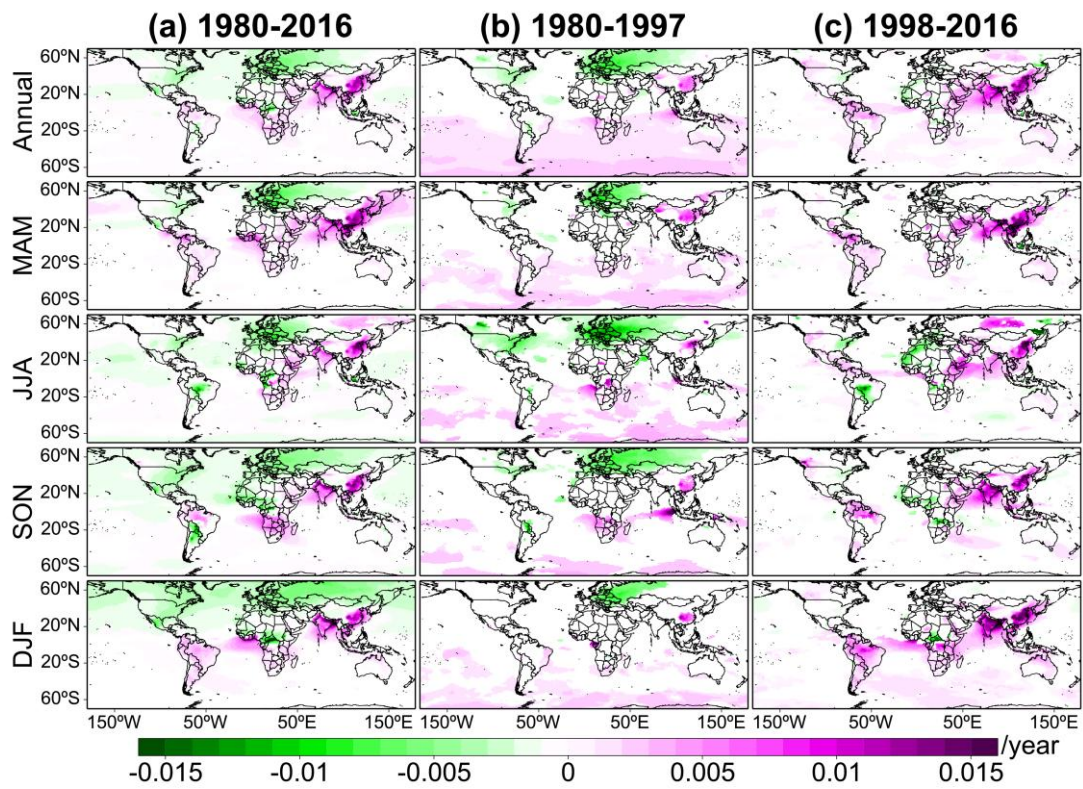
1576

1577

1578

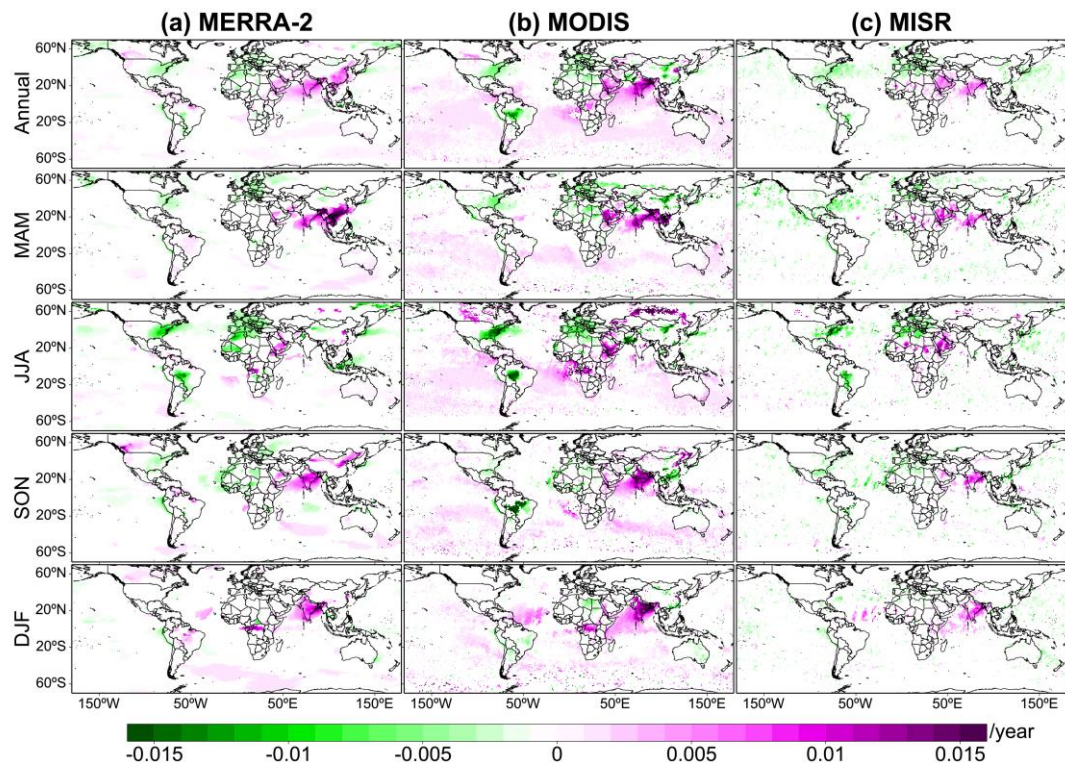
1579

Figure 5. Temporal evolution of regional monthly averaged AOD for the 12 regions of interest. Each year is represented by an irregular ring with 12 directions. Each direction of the ring represents a specific month; the distance from the center of the ring represents the regional monthly mean AOD value; and the color of the ring represents the year. A special ring colored cyan represents the monthly mean AOD for the period 1980–2016.



1580
 1581
 1582
 1583
 1584
 1585

Figure 6. Spatial distributions of the linear trends in annual and seasonal MERRA-2 AOD calculated from the time series value of the de-seasonalized monthly anomaly during (a) 1980–2016, (b) 1980–1997, and (c) 1998–2016. Only trend values with statistical significance at the 95% confidence level are shown.



1586

1587

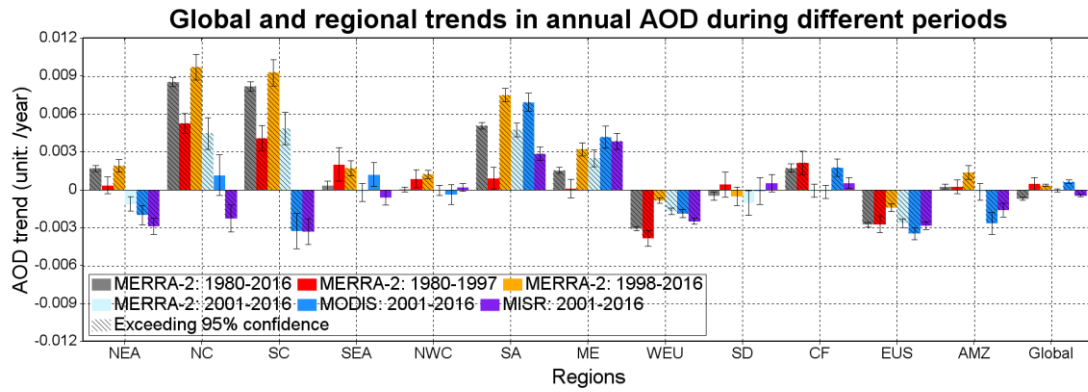
1588

1589

1590

1591

Figure 7. Spatial distributions of annual and seasonal trends in AOD calculated from the time series value of the de-seasonalized monthly anomaly from (a) MERRA-2, (b) MODIS/Terra, and (c) MISR between 2001 and 2016. Only trend values with statistical significance at the 95% confidence level are shown.



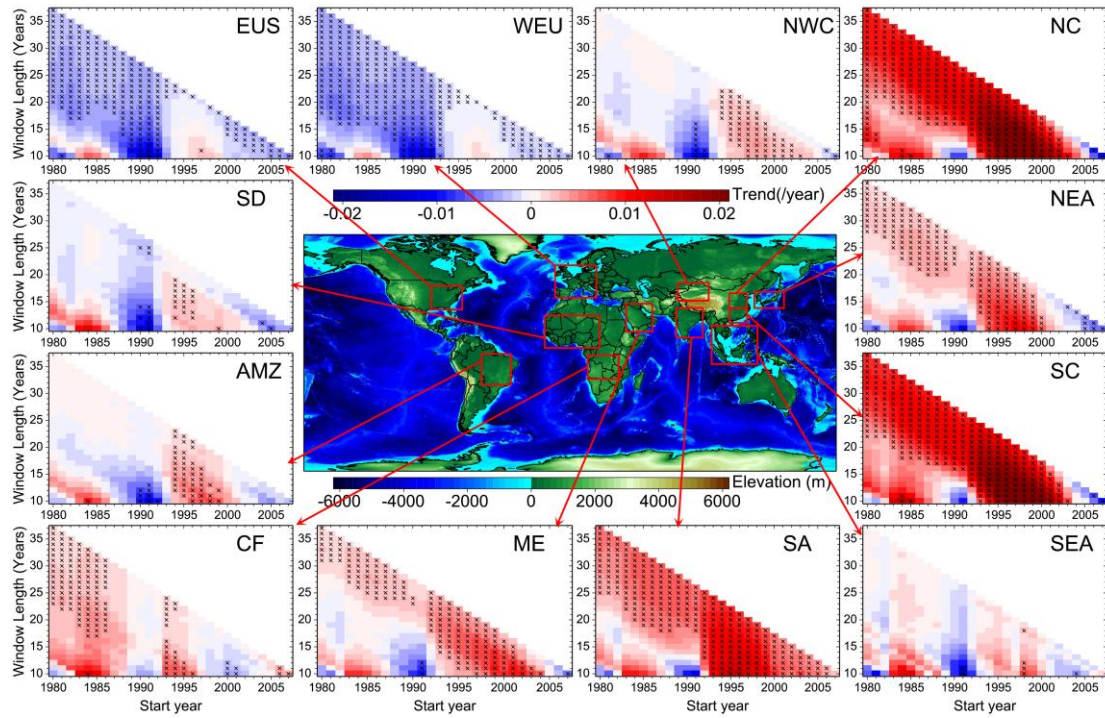
1592

1593

Figure 8. Inter-comparisons of global and regional annual trends in AOD calculated from the time series value of the de-seasonalized monthly anomaly of MERRA-2, MODIS/Terra and MISR, during the four periods of 1980–1594 1980–1997, 1998–2016, and 2001–2016. Error bars represent the uncertainty associated with the calculated 1595 1596 trend. The trend bars with shadow indicate statistical significance at the 95% confidence level.

1597

1598



1599

1600

1601

1602

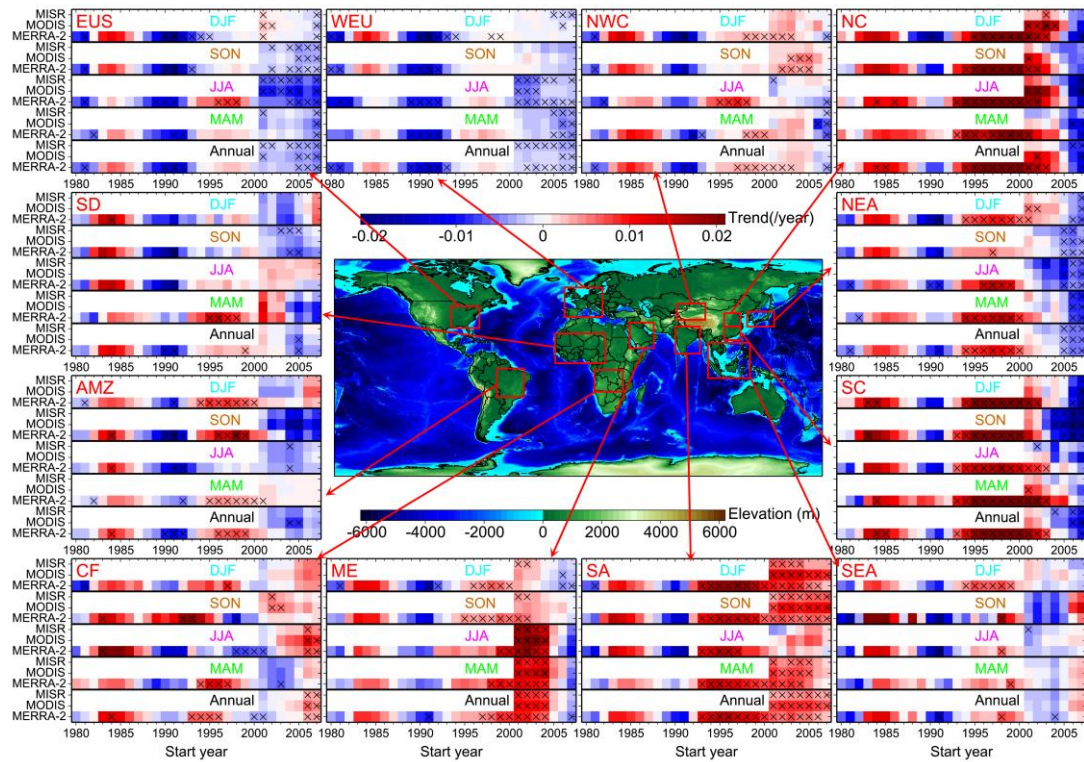
1603

1604

1605

1606

Figure 9. Sliding-window trend analyses of the annual mean MERRA-2 AOD from 1980 to 2016 over the 12 ROIs (see Fig. 1 for names and locations of regions), with at least 10 years used to calculate trends. The x-axis and y-axis indicate the start year and the length of the time series to calculate the trend, respectively. The colors of rectangles represent the intensity of the trend (units: /year), and those with black 'x' signs indicate linear trends above the 95% significance level.



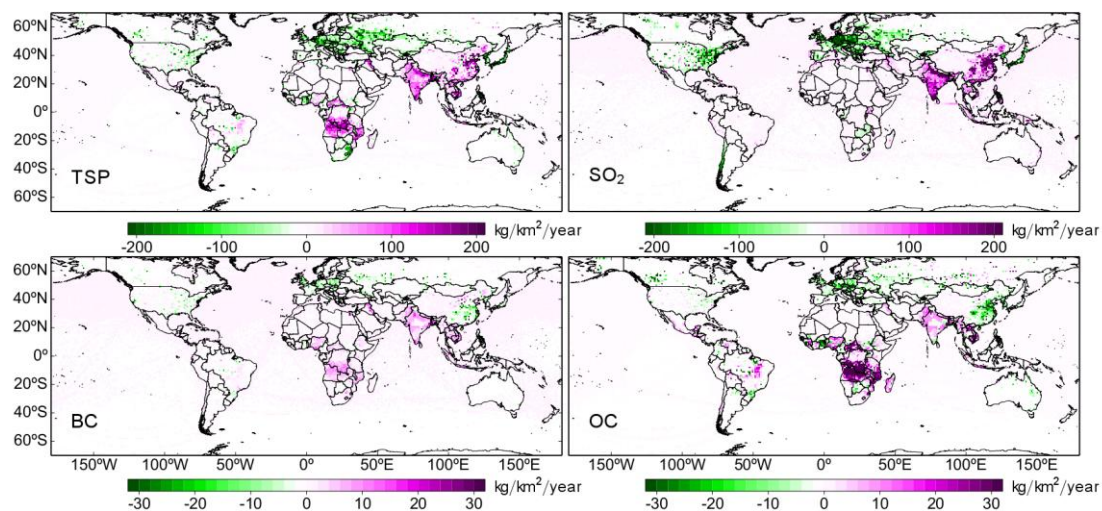
1607

1608

Figure 10. Temporal evolution of sliding decadal trends in the annual and seasonal mean AOD from MERRA-2, MODIS/Terra and MISR over the 12 ROIs. The trends were calculated for each 10-year interval from 1980 to 2007 for MERRA-2, and from 2001 to 2007 for MODIS/Terra and MISR. The colors of the rectangles represent the intensity of the decadal trend (units: /year), and those with black 'x' signs indicate linear trends above the 95% significance level.

1613

1614

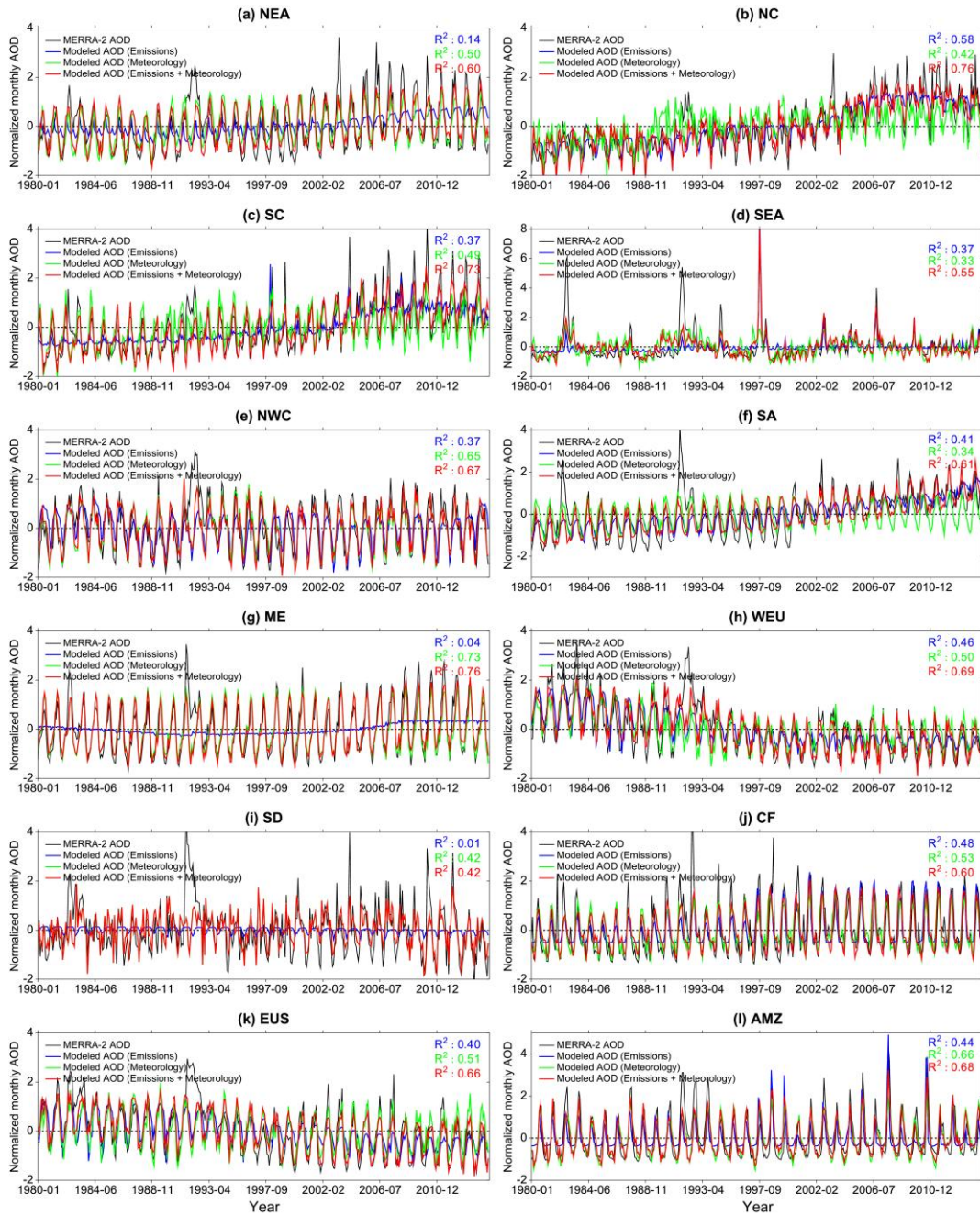


1615

1616 **Figure 11.** Spatial distributions of linear trends (units: kg/km²/year) in total anthropogenic emissions of total
 1617 suspended particles (TSP), SO₂, black carbon (BC), and organic carbon (OC) during 1980–2014 derived from the
 1618 Peking University emissions inventory (<http://inventory.pku.edu.cn/>) (Huang et al., 2014). Only linear trend values
 1619 with statistical significance at the 95% confidence level are shown.

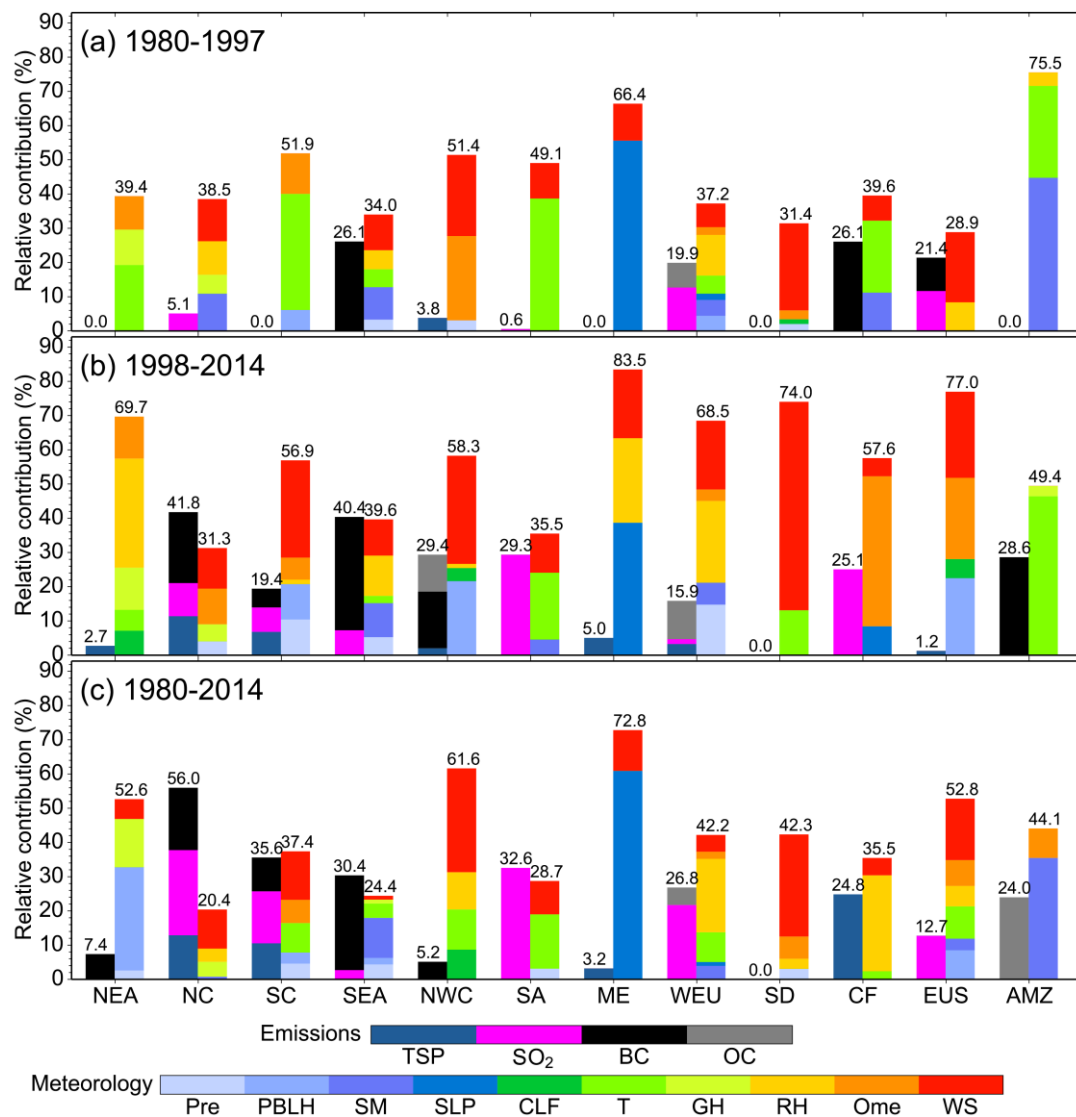
1620

1621



1622
 1623
 1624
 1625
 1626
 1627
 1628

Figure 12. Time series of MERRA-2 (in black) and modeled AOD monthly normalized anomalies from 1980 to 2014 over the 12 regions of interest. The coefficient of determination (R^2) of the regression fit of the stepwise MLR model with emission factors (in blue), meteorology (in green), and both emissions and meteorology (in red) as predictors are given in the top-right of each panel.



1629
 1630
 1631
 1632
 1633
 1634
 1635
 1636
 1637
 1638

Figure 13. The LMG method–estimated relative contributions (%) of total variances in the stepwise MLR model explained by the local emission factors (left-hand bars) and meteorological variables (right-hand bars) over the 12 regions of interest during three periods: (a) 1980–1997 (top panel); (b) 1998–2014 (middle panel); and (c) 1980–2014 (bottom panel). Note that meteorological parameters were combined as follows: temperature, T (Ts, T₈₅₀, T₇₀₀, T₅₀₀, dT_{900-s}, dT_{850-s}); geopotential height, GH (GH₈₅₀, GH₇₀₀, GH₅₀₀); relative humidity, RH (RH_s, RH₈₅₀, RH₇₀₀, RH₅₀₀); vertical velocity, Ome (Ome₈₅₀, Ome₇₀₀, Ome₅₀₀); and wind speed, WS (U₈₅₀, U₇₀₀, U₅₀₀, V₈₅₀, V₇₀₀, V₅₀₀, WS_s, WS₈₅₀, WS₇₀₀, WS₅₀₀, VWS₅₀₀₋₈₅₀). Refer to Table S3 for the detailed relative contributions of each variable in the stepwise MLR models.